Full Modeling and Parameter Compression Methods in configuration space for DESI 2024 and beyond

```
S. Ramirez-Solano, 1 M. Icaza-Lizaola, 2 H. E. Noriega, 3,1
```

- K. Honscheid, 21,22,23 C. Howlett, S. Juneau, 10 Y. Lai, 24
- M. Landriau[®], ⁴ M. Manera[®], ^{25,26} M. Maus, ²⁷ R. Miquel, ^{28,26}
- E. Mueller,²⁹ A. Muñoz-Gutiérrez,¹ A. D. Myers,³⁰
- S. Nadathur[®], ¹⁷ J. Nie[®], ³¹ W. J. Percival[®], ^{32,33,34} C. Poppett, ^{4,35,27} M. Rezaie[®], ³⁶ G. Rossi, ³⁷ E. Sanchez[®], ³⁸
- D. Schlegel,⁴ M. Schubnell,^{39,6} H. Seo[®],⁴⁰ D. Sprayberry,¹⁰
- G. Tarlé, 6 L. Verde, 28,20 B. A. Weaver, 10
- R. H. Wechsler, 12,41,13 S. Yuan, 13 P. Zarrouk, 42 H. Zou, 31

M. Vargas-Magaña[®], ¹ S. Fromenteau[®], ³ A. Aviles[®], ³

F. Rodríguez-Martínez, J. Aguilar, S. Ahlen, O. Alves,

S. Brieden[®], D. Brooks, T. Claybaugh, S. Cole[®], A. de la Macorra[®], Arjun Dey[®], B. Dey[®], P. Doel, 8

K. Fanning, 12,13 J. E. Forero-Romero, 14,15 E. Gaztañaga, 16,17,18

H. Gil-Marín[®], ^{19,16,20} S. Gontcho A Gontcho[®], ⁴

E-mail: sadiramirez@estudiantes.fisica.unam.mx

Abstract. In the contemporary era of high-precision spectroscopic surveys, led by projects like DESI, there is an increasing demand for optimizing the extraction of cosmological information from clustering data. This work conducts a thorough comparison of various methodologies for modeling the full shape of the two-point statistics in configuration space. We investigate the performance of both direct fits (Full-Modeling) and the parameter compression approaches (ShapeFit and Standard). We utilize the ABACUS-SUMMIT simulations, tailored to exceed DESI's precision requirements. Particularly, we fit the two-point statistics of three distinct tracers (LRG, ELG, and QSO), by employing a Gaussian Streaming Model in tandem with Convolution Lagrangian Perturbation Theory and Effective Field Theory. We explore methodological setup variations, including the range of scales, the set of galaxy bias parameters, the inclusion of the hexadecapole, as well as model extensions encompassing varying n_s and allowing for w_0w_a CDM dark energy model. Throughout these varied explorations, while precision levels fluctuate and certain configurations exhibit tighter parameter constraints, our pipeline consistently recovers the parameter values of the mocks within 1σ in all cases for a 1-year DESI volume. Additionally, we compare the performance of configuration space analysis with its Fourier space counterpart using three models: PyBird, FOLPS and Ve-LOCILEPTORS, presented in companion papers. We find good agreement with the results from all these models.

Keywords: Large-Scale Structure, Full Shape analysis.

\mathbf{C}	ontents	
1	Introduction	1
2	Simulations mocks and covariance 2.1 Mock Data 2.2 Covariance Mocks	4 4 5
3	Modeling Redshift Space Distortions with GSM-EFT 3.1 Gaussian streaming model 3.2 Neural Network Accelerators	5 6
4	Extracting Cosmological Information from Clustering 4.1 Classical methodology 4.2 ShapeFit methodology 4.2.1 ShapeFit in Configuration Space 4.3 Inferring cosmological parameters from compressed parameters 4.4 Full Modeling in Configuration space 4.5 GSM-EFT code for compressed and direct fits: Users guide 4.6 Likelihood and Priors	8 9 11 13 15 16 17
5		19 19 19 22 26 26 27 29 31
6	Comparisons with others Effective Field Theory models 6.1 Comparison with EFT models in Fourier Space 6.2 Comparison with EFT models in Configuration space with DesiLike	35 38 39
7	Conclusions	40
8	Data Availability	43

1 Introduction

A Author Affiliations

The study of the large-scale structure (LSS) of the Universe is a fundamental pillar in modern cosmology, and it provides an important observable to investigate its subsequent evolution over time. Observations of the LSS through the distribution of galaxies enable the extraction

43

of valuable information that can be used to compare to theoretical predictions and impose constraints on cosmological parameters.

Spectroscopic galaxy surveys collect data on the angular position and redshift of millions of galaxies across a wide range of cosmic epochs. Two key phenomena, which have left distinct features in the clustering of galaxies, are extensively utilized for extracting cosmological insights.

The first phenomenon involves fluctuations in the matter density, arising from acoustic density waves in the primordial plasma of the early universe. These effects are discernible through the peak of the correlation function at comoving scales of $\sim 100\,h^{-1}\,\mathrm{Mpc}$, and are commonly referred to as baryon acoustic oscillations (BAO).

The second key observable arises from apparent anisotropies in the clustering of galaxies along the line-of-sight (LoS), attributed to their peculiar velocities. This phenomenon is known as redshift space distortions (RSD). While RSD introduce complexities in interpreting the observed positions of galaxies as a 3-D map, they also provide a unique opportunity to access information concerning the growth rate of the LSS.

In the last decade, the clustering of galaxies has been analyzed through data collected by spectroscopic galaxy surveys such as the 2dF Galaxy Redshift Survey (2dFGRS) [1, 2], the Baryon Oscillation Spectroscopic Survey (eBOSS) [5, 6], or the Dark Energy Survey (DES) [7, 8]. These surveys have significantly increased both precision and volume over the years. At the time of publication, the next generation of surveys is being developed with the EUCLID mission [9, 10] launching in the summer of 2023, and The Rubin Observatory Large Synoptic Survey Telescope (LSST) [11] survey expected to have its first light in the summer of 2024. Simultaneously, the Dark Energy Spectroscopic Instrument (DESI) 1 [12–15] is currently ongoing and is mapping the universe over an unprecedented range of 14,000 deg² with an effective volume of $40 (h^{-1} \,\text{Gpc})^3$, improving the number of observed galaxies by an order of magnitude compared to previous surveys. Plans for a continuing survey, DESI-II [16], that will focus on the z > 2 universe are being made, and observations are expected to start in 2026.

DESI targets different tracers of matter at various redshifts, including emission line galaxies (ELG) [17] at 0.6 < z < 1.6, luminous red galaxies (LRG) [18] at 0.3 < z < 1.0, and quasars at (QSO) 0.9 < z < 2.1 [19] during the dark-time program. The exceptional accuracy of these surveys will necessitate models capable of predicting clustering statistics with great precision.

Perturbation theory (PT) when applied to data in either the Lagrangian approach [20–26] or Eulerian approach [27–30] has demonstrated to accurately predict galaxy densities, velocities and redshift-space distortions within the quasi-linear regime. Recently, PT has been complemented with effective field theory (EFT) [31–36] parameters to account for backreaction of small scale physics over quasi-linear scales. This has proven effective in confronting theoretical predictions of clustering statistics with observations or simulations. In this work, we follow the Lagrangian PT (LPT)/EFT approach [35, 37–40].

In anticipation of the DESI Year 1 data release, the DESI collaboration aims at testing systematic effects of their methodologies using the new ABACUS-SUMMIT [41] suite of simulations, which are designed to surpass the resolution and volume requirements for cosmological simulations within DESI. Currently, four perturbations approaches for modeling the redshift space clustering statistics are being analyzed and compared within the DESI collaboration.

¹www.desi.lbl.gov

These models include the configuration space EFT-GSM [42] code, which is utilized throughout this work, as well as three Fourier space codes, namely PYBIRD [43–46], FOLPS ν [47, 48] and VELOCILEPTORS [49–51]. A comparison for the three Fourier space codes can be found in the companion paper [52] and, in this paper, we compare our configuration space model and the other Fourier space models.

In this work, we assess potential systematics within the pipeline of our EFT-GSM model for the DESI first-year data release. EFT-GSM model by construction is designed to model the redshift space correlation function up to one-loop corrections working on the LPT framework and using the Gaussian Streaming Model [35, 53–56], in addition to EFT parameters. This framework allows us to model small-scale physics down to scales as low as $20\,h^{-1}$ Mpc, where non-linear processes appear. Our methodology has been introduced and optimized with neural networks in [42] we test it using the Nseries simulations [4], a suite of N-body simulations that were designed to analyze the eBOSS data and have a lower resolution than the ABACUS-SUMMIT simulations. The main difference between our EFT-GSM methodology and the other three methodologies is that we fit the correlation function directly, whereas the other methodologies work in Fourier space.²

Two different approaches have been used for extracting cosmological information from the shape of two-point statistics, the compressed methodologies (as the Standard and Shape Fit methodologies), and the direct fits (also called Full-Modelling). The *Standard* methodology employed for analyzing the clustering of redshift space tracers throughout SDSS-III BOSS [3, 57, 58] and SDSS-IV eBOSS [59–61] requires a one-time calculation of the linear power spectrum within a chosen fiducial cosmology. This power spectrum is then coupled with a PT framework, and the relevant cosmological information are compressed into three free parameters: the linear growth rate of structures $f\sigma_8$ and two scaling parameters, parallel and perpendicular to the line of sight α_{\perp} and α_{\parallel} , that parameterize the Alcock-Paczynski effect [62].

The ShapeFit methodology of [63] suggests adding a new free parameter to the Standard compressed methodology of BOSS and eBOSS, this parameter models the transition of the linear power spectrum from large to small scales, by including a new effective parameter m, that modifies the slope of the linear power spectrum. The agnostic nature of compressed methodologies, like the Standard approach utilized for BOSS and eBOSS, or the more recent ShapeFit methodology, exhibit a relatively high degree of model independence compared to those derived from Full Modeling analysis. Moreover, their significantly lower computational costs make them more appealing from a practical standpoint. Although the ShapeFit methodology has been tested in Fourier space [e.g. 63], its performance in configuration space is still an ongoing area of investigation.

An alternative approach opposed to the compressed nature of the *Standard* and Shape Fit methodologies is to directly explore the posterior distribution of all cosmological parameters. This involves calculating the linear power spectrum at each step of the Markov Chain Monte Carlo (MCMC) exploration. Referred to as the *Full Modeling* or *Direct Fit* approach, it offers the advantage of tighter constraints on cosmological parameters, which are directly constrained. This method has been applied in the analysis of both BOSS [64, 65] and eBOSS [66, 67]. While these *Full Modeling* approaches can be resource-intensive to construct, advancements in computing capabilities and the evolution of new machine-learning algorithms have accelerated analytical calculations in recent years. Consequently, it has become feasible

²Reference [46] also works with the correlation function, through Fourier transforming the power spectrum obtained with PyBird.

to model the full shape of the correlation function or power spectrum and simultaneously vary cosmological, bias, and EFT (Effective Field Theory) parameters.

Throughout this work, we evaluate the performance of the three methodologies for extracting cosmological information *Standard* and *Shape Fit*, and *Full Modeling*), and we compare the analysis of these three methods across a range of conditions and across different DESI tracers to have a better understanding of the differences among them.

This paper gives support to the *DESI 2024: Full-Shape analysis from galaxies and quasars* [68] which is part of the DESI Year 1 main results [69–74].

The structure of this paper is as follows. We begin in section 2 by introducing and describing the simulations used throughout this work. Then in Section 3 we describe the theory behind the EFT-GSM model. Section 4 describes the implementation of our three different methods: the Standard methodology, the Shape-Fit methodology and the Full Modeling methodology. The material presented up until this point is not new to this work. So, a busy reader can directly skip sections 3 and 4. Section 5 shows the results of our pipeline for these three distinct methodologies, and explores different configurations of our model. First, we define our baseline analysis and investigate how different variations to it affect our results, these variations include differences in the fitting range explored and different settings for the galaxy bias terms. We continue by exploring the effects on our models constraints under different extensions to our baseline configuration, this extensions include adding the hexadecapole of the correlation function, extending the parameter space explored by adding n_s as a free parameter, and including the parameters of the equation state of dark energy as free parameters. We finalize this section by presenting the results for our three different tracers and presenting a joint analysis where all tracers are analyzed simultaneously. The last subsection presents the comparison between Shape-Fit and Full Modeling methodologies for our baseline analysis. Finally, Section 6 has a comparison between our GSM-EFT model and other EFT models in Fourier space and configuration space. The conclusions of this paper are in section 7.

2 Simulations mocks and covariance

As we have stated, the main goal of our work is to test the performance and analyze the potential systematics of our methodology on a mock representation of the DESI ELG, LRG, and QSO surveys. We begin our work in section 2.1 by introducing our mock datasets, generated with the ABACUS-SUMMIT simulation. The various analyses presented in this work involve estimating the likelihood that the correlation functions produced by our EFT-GSM model agree with those measured from the ABACUS-SUMMIT simulation across a range of parameters and across different model configurations. The computation of these likelihoods requires estimates of the covariance of our correlation function. The methodology and simulations we utilize to compute this covariance are introduced in Section 2.2.

2.1 Mock Data

In this study, we test the correlation function model using a set of 25 cubic boxes, with a volume of $(2 h^{-1} \text{Gpc})^3$, which were generated utilizing the ABACUS-SUMMIT high-accuracy N-body simulations [41]. Consequently, the combined volume extends to $200 h^{-3} \text{Gpc}^3$. Each ABACUS-SUMMIT box contains a total of 6912^3 particles, with each particle carrying a mass of $2 \times 10^9 h^{-1} \text{M}_{\odot}$. These simulations adopt the cosmological parameters from Planck 2018 [75]:

h = 0.6736, ω cdm = 0.1200, ω _b = 0.02237, $\ln(10^{10}A_s) = 3.0364$, $n_s = 0.9649$, $M_{\nu} = 0.06 \,\text{eV}$, $w_0 = -1$.

Our mocks are based on HOD fitted on the Survey Validation 3 (SV3) spectroscopic data from DESI and consists of three independent sets of catalogs, each representing a different tracer: LRG at z=0.8, ELG at z=1.1, and the QSO at z=1.4. In order to populate our simulations with galaxies, we utilize the halo occupation distribution (HOD) methodology described in [76] for ELG and in [77] for LRG and QSO. The HOD models are calibrated using small-scale wedges (below $5\,h^{-1}{\rm Mpc}$) in combination with large-scale bias evolution information, whenever the former is available. These calibrations are done independently for each snapshot of the simulation.

Through this work we utilize the correlation function that we measure from these Abacus mock simulations, these correlation functions are utilized to fit the parameters of our models. Our estimates of the correlation function are defined as the mean of these 25 mock realizations for each tracer, where the s-bins in our analysis are spaced at intervals of $\Delta s = 4 \ h^{-1}{\rm Mpc}$. In Figure 1 we show the mean of the ABACUS multipoles for $\ell = 0, 2, 4$ for the three tracers, LRG (left panel), ELG(intermediate panel) and QSO(right panel).

2.2 Covariance Mocks

One common approach for computing covariance matrices is to utilize the correlation function measured from thousands of different realizations. These simulations are usually computed by methods that are optimized for efficiency rather than accuracy. In this work, we utilize 1000 approximate mocks generated with the Extended Zel'dovich methodology [78] with the same cosmology of ABACUS-SUMMIT. We compute the covariance matrix C of each tracer between bins i and j, using the 1000 EZ mocks, as follows:

$$C_s^{(ij)} = \frac{1}{N_{\text{mocks}} - 1} \sum_{m=1}^{N_{\text{mocks}}} (\xi_i^m - \bar{\xi}_i) (\xi_j^m - \bar{\xi}_j), \qquad (2.1)$$

where $N_{\text{mocks}} = 1000$ represents the total number of mocks, and $\bar{\xi}_i$ denotes the average of the i^{th} bin in the analysis. The Hartlap factor induces a slight change in the inverse covariance matrix, typically around 0.94 to 0.95, depending on the scales. Hence, its influence in this study is thought to be negligible, as the values vary by less than 0.5%.

In this work, we use three re-scaling for the covariance: without re-scaling that corresponds to a volume of one simulation $8 h^{-3} \,\mathrm{Gpc^3}$, re-scaling by a factor 1/5 that corresponds to a volume of $V_5 = 40 \,h^{-3} \,\mathrm{Gpc^3}$ and re-scaling 1/25 corresponding to $V_{25} = 200 \,h^{-3} \,\mathrm{Gpc^3}$. In Figure 1 we show as shaded region the square root of the diagonal terms of the EZ mocks covariance without re-scaling for the three tracers, LRG (left panel), ELG (intermediate panel), and QSO (right panel). We also add error bars corresponding to the 1/25 re-scaled covariance.

3 Modeling Redshift Space Distortions with GSM-EFT

In this section, we introduce the methodology we follow to compute the theoretical templates of the correlation function using our EFT-GSM model. We begin in section 3.1 by briefly introducing the theoretical background behind GSM, which in addition to the convolution Lagrangian perturbation theory (CLPT) and EFT, allows us to model the redshift space two-point correlation function. Then, in section 3.2, we summarize the methodology followed to build the machine learning emulators that enhance the efficiency and speed of our analysis.

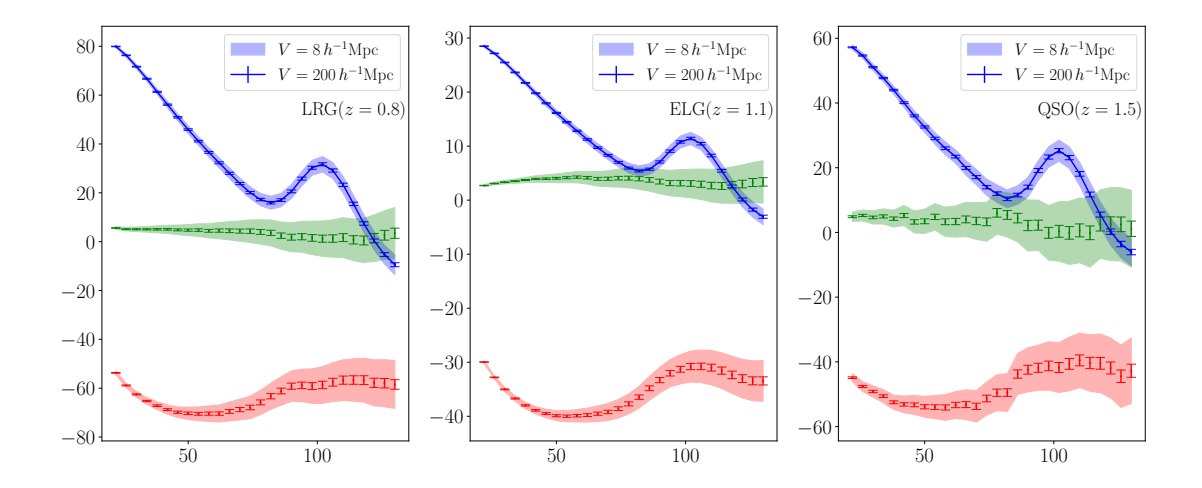


Figure 1. ABACUS-SUMMIT simulations for the multipoles of the correlation function for three tracers: LRGs (left), ELGs (middle), and QSOs (right). The shadow region represents the errors of the covariance matrix, while the error bar represents the same error re-scaled by $1/\sqrt{25}$.

3.1 Gaussian streaming model

The GSM-EFT code³ [79] is based on the LPT approach, where each cold dark matter fluid element position is parameterized by its initial location \mathbf{q} and the Lagrangian displacement field $\mathbf{\Psi}(\mathbf{q},t)$, as $\mathbf{x}(\mathbf{q},t) = \mathbf{q} + \mathbf{\Psi}(\mathbf{q},t)$. Here, the displacement is governed by the Euler equation $\partial_t^2 \mathbf{\Psi} + 2H \partial_t \mathbf{\Psi} = -\frac{1}{a^2} \nabla \mathbf{\Phi}(\mathbf{q} + \mathbf{\Psi})$ and, which we solve perturbatively by expanding the displacement as,

$$\Psi(\mathbf{q}) = \Psi^{(1)}(\mathbf{q}) + \Psi^{(2)}(\mathbf{q}) + \cdots . \tag{3.1}$$

Since we work with the observed position s, we must consider the LoS anisotropies introduced by particles' peculiar velocities. By doing this, the map between Lagrangian and redshift space coordinates is given by,

$$s = q + \Psi + \hat{n}\frac{\dot{\Psi} \cdot \hat{n}}{H}, \tag{3.2}$$

where $\hat{\boldsymbol{n}}$ is a unitary vector on the LoS direction. The correlation function in redshift space is obtained through the conservation of the number of tracers X, expressed as $\begin{bmatrix} 1 + \delta_s(\boldsymbol{s}) \end{bmatrix} d^3s = \begin{bmatrix} 1 + \delta_X(\boldsymbol{x}) \end{bmatrix} d^3x$. Following [54, 80], one obtains

$$1 + \xi_s(\mathbf{s}) = \int \frac{d^3k}{(2\pi)^3} d^3x \, e^{i\mathbf{k}\cdot(\mathbf{s}-\mathbf{r})} \exp\left[\sum_{n=0}^{\infty} \frac{(-i)^n}{n!} k_{i_1} \cdots k_{i_n} \mathcal{C}_{i_1 \cdots i_n}^{(n)}(\mathbf{r})\right], \tag{3.3}$$

³https://github.com/alejandroaviles/gsm

where the relation between cumulants C and moments Ξ , of the pairwise density weighted velocity distribution function, up to second order is given by

$$\mathcal{C}^{(0)}(\mathbf{r}) = \log[1 + \xi(r)],\tag{3.4}$$

$$C_i^{(1)}(\mathbf{r}) = \frac{\Xi_i^{(1)}(\mathbf{r})}{1 + \xi(\mathbf{r})} \equiv v_{12,i}, \tag{3.5}$$

$$C_{ij}^{(2)}(\mathbf{r}) = \frac{\Xi_{ij}^{(2)}(\mathbf{r})}{1 + \xi(\mathbf{r})} - C_i^{(1)}(\mathbf{r})C_j^{(1)}(\mathbf{r}) \equiv \hat{\sigma}_{12,ij}^2 - v_{12,i}v_{12,j} = \sigma_{12,ij}^2, \tag{3.6}$$

where $\xi(r)$ is the tracers real space correlation function and the moments are given by

$$\Xi_{i_1\cdots i_n}^{(n)}(\mathbf{r}) = \langle (1+\delta(\mathbf{r}))(1+\delta(0))\Delta u_{i_1}\cdots \Delta u_{i_n} \rangle, \tag{3.7}$$

where $\Delta u_i = u_i(\mathbf{r}) - u_i(0)$, and $u_i = \hat{n}_i \hat{n}_j \dot{\Psi}_j / H$ is the peculiar velocity field along the LoS in Hubble function units.

We have further introduced the pairwise velocity along the LoS $v_{12,i}$, and the pairwise velocity dispersion moment and cumulant, $\hat{\sigma}_{12,ij}^2$ and $\sigma_{12,ij}^2$, respectively. Throughout this work we employ CLPT to compute the moments [37–39, 81–83]. A detailed description of our implementation of CLPT into the GSM can be found in [42]. The precise equations we use are given below, in §4.2.1.

By truncating the sum in the exponential in eq. (3.3) up to the second moment, we obtain the standard expression for the Gaussian Streaming Model correlation function:

$$1 + \xi_s(s_{\parallel}, s_{\perp}) = \int_{-\infty}^{\infty} \frac{dr_{\parallel}}{\left[2\pi\sigma_{12}^2(r, \mu)\right]^{1/2}} \left[1 + \xi(r)\right] \exp\left[-\frac{\left(s_{\parallel} - r_{\parallel} - \mu v_{12}(r)\right)^2}{2\sigma_{12}^2(r, \mu)}\right], \quad (3.8)$$

where the pairwise velocity and pairwise velocity dispersion are projected along the separation vector: $v_{12} = v_{12,i}\hat{r}_i$ and $\sigma_{12} = \sigma_{12,i}\hat{r}_i\hat{r}_j$. The labels $_{\parallel}$ and $_{\perp}$ are used to indicate components parallel and perpendicular to the LoS direction and μ is the cosine of the angle between the separation direction of the two galaxies and the LoS.

As noticed in [39], the second moment of the density distribution is very sensitive to small scale physics, hence the velocity dispersion should be corrected by an EFT parameter, such that

$$\sigma_{12}^2(r) \to \sigma_{12}^2(r) + \sigma_{\text{EFT}}^2 \frac{1 + \xi^{\text{ZA}}(r)}{1 + \xi(r)},$$
 (3.9)

where $\xi^{\mathrm{ZA}}(r)$ is the Zel'dovich Approximation matter correlation function. One may notice that for sufficiently large r, one has $1+\xi(r)\approx 1$, recovering the phenomenological description of the dispersion due to the Fingers of God effect: $\sigma^2_{\mathrm{EFT}}(1+\xi^{\mathrm{ZA}}(r))/(1+\xi(r))\to\sigma^2_{\mathrm{FoG}}$. In our final modeling we will use a second counterterm as shown in section 4.2.1.

To compute the real space correlation function ξ , the pairwise velocity v_{12} and velocity dispersion σ_{12} we utilize CLPT/EFT [35, 38] as implemented in [39]. Specifically, we use eqs. (4.20), (4.23) and (4.24) displayed below. Those equations also specify how the biases and counter-terms (apart from σ_{EFT}^2 introduced above) enter our correlation function modeling.

3.2 Neural Network Accelerators

The methodology outlined in the previous section has been implemented into our GSM-EFT code, enabling the prediction of the galaxy correlation function for a given set of cosmological

parameters in just a couple of seconds. Despite this relative speed, the sheer volume of evaluations required for a MCMC analysis typically falls on the order of 10^5 . Combined with the numerous independent MCMC analyses presented throughout this work, this incentivizes us to accelerate the evaluation time of our models using neural network emulators.

These emulators work as surrogate models that learn to predict the correlation function of the parameters in approximately 0.015 seconds, resulting in a speedup of two orders of magnitude once trained. Throughout this work, we construct a distinct neural network for each redshift and for each multipole of the correlation function. Each of these emulators requires around 30 minutes to train. Our neural network approach is an adaptation of the code presented in [84]⁴, which we modified to work in configuration space instead of Fourier space, as originally designed. The neural network architecture utilizes a Multi-Layer Perceptron with four hidden layers, each containing 128 neurons. In this work, we construct one individual neural network per multipole.

Figure 2 shows a scheme of our methodology. We implemented a decreasing learning rate strategy, starting from 10^{-2} and decreasing to 10^{-6} in steps of one order of magnitude. We reduce the learning rate with a patience of 1000 epochs, i.e., if there is no improvement for 1000 epochs. At each step, the batch size is doubled. Additionally, we employ the following activation function, as suggested by [84, 85]:

$$a(X) = \left[\gamma + (1 + e^{-\beta \odot X})^{-1} (1 - \gamma)\right] \odot X. \tag{3.10}$$

These emulators were first introduced and thoroughly tested in [42]. Here, we provide a brief description of the emulator methodology, with a reference to our original work for a more detailed discussion.

To train a neural network, we initially generate 60,000 points in parameter space. This holds true for most results presented in this work, with the exception of certain extensions to our baseline analysis where the models are more complex, which requires a larger training set, as discussed in sections §5.2.2 and §5.2.3 below. Of these points, 50,000 are utilized as the training data, fed into the training algorithm. Additionally, we allocate 5,000 points as the validation set, which the neural network employs to assess the accuracy of the model at each training epoch. Based on the performance of the model, the algorithm may adjust the learning rate or finalize the model. The remaining 5,000 points constitute the test set, which we employ to evaluate the model's accuracy on unseen data. All three sets are independently generated using a Korobov design [86] to construct uniform samples in a large dimensional space.

4 Extracting Cosmological Information from Clustering

As we illustrate in Figure 3, we can distinguish two different approaches for extracting cosmological information from clustering:

1) Compressed approaches [e.g. 3, 57–61, 87] shown in the right panel, where the philosophy is to extract the cosmological information from the measured clustering data $\{\xi(s,\mu), p(k,\mu)\}$ through the constraints on compressed variables, Θ_{obs} , that are related with physical observables. These compressed variables are further translated into constraints to cosmological parameters using different cosmological models. In this approach, the constraints on the physical observables are proven to be mildly affected by the cosmological model and, for this

⁴Their code is publicly available and can be found at https://github.com/sfschen/EmulateLSS/tree/main

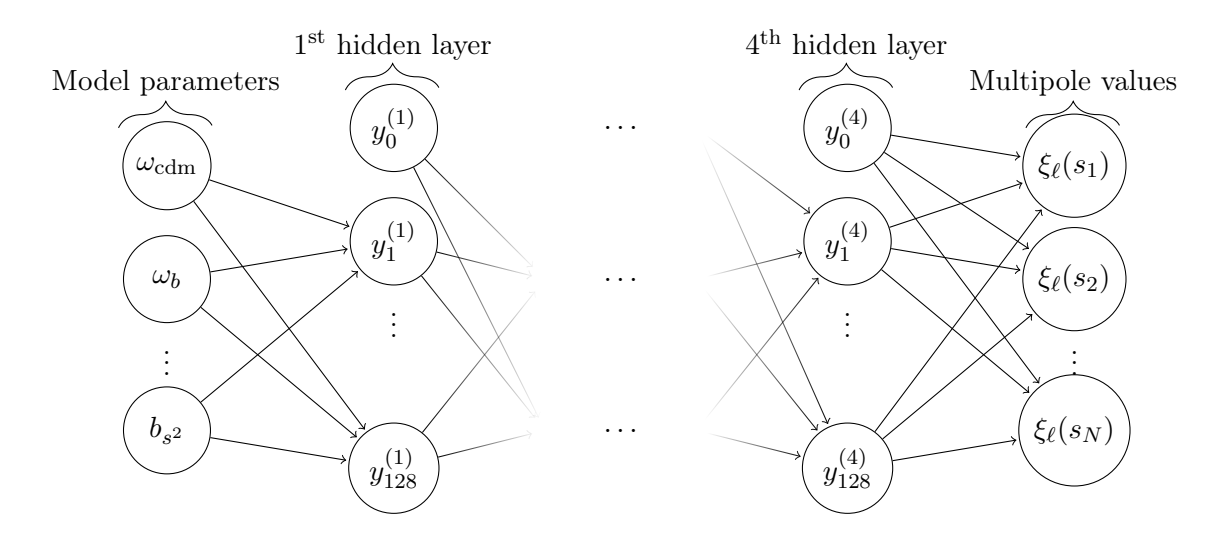


Figure 2. Architecture representation of our three Neural Networks, one identical for each multipole $(\ell = 0, 2, 4)$ of the correlation function.

reason, it is considered agnostic to the cosmological model. 2) Full Modeling or Direct fits [e.g. 88–93] shown in the left panel, where the extraction of cosmological information from the measured clustering data $\{\xi(s,\mu),p(k,\mu)\}$ is done by comparing them directly with theoretical predictions computed for each cosmological model constraining directly the cosmological (and nuisance) parameters θ_{Ω} of the model, without any intermediate step. Full Modeling has received increasing attention post-Stage-III survey's period, given the optimization of models and codes and the use of sophisticated statistical tools in the last decade, that allows us to compute efficiently the posterior in a highly dimensional space while varying directly the cosmological and nuisance parameters of the model.

Within the compressed approaches, we can distinguish two methodologies: 1) Classical or Standard methodology proposed and developed within spectroscopic survey collaborations (as SDSS-II, BOSS and eBOSS), which is based on compressing the cosmological information into measuring physical observables denoted as BAO and RSD; and 2) ShapeFit [63] approach that is an extension of the classical approach aiming to achieve more constraining power through the inclusion of two additional parameters that bring information about the early universe. In this section, we briefly describe the three different approaches and their implementation in configuration space for the model used in this work, the GSM-EFT.

4.1 Classical methodology

The Classical or Standard methodology

is based on a *fixed template*, which is generated using a particular perturbative model, computed for a fixed reference cosmology. The *fixed template* is modified by three compressed variables associated with late-time dynamics:

$$\{\alpha_{\parallel}, \alpha_{\perp}, f\sigma_8\},\tag{4.1}$$

 α_{\perp} and α_{\parallel} parameterize distortions parallel and perpendicular to the line of sight and control the variations along the r-axis. The $f\sigma_8$ parameter varies the relative amplitude of our multipoles. The quantity $f\sigma_8$ is the product of the linear growth rate of structures f defined by,

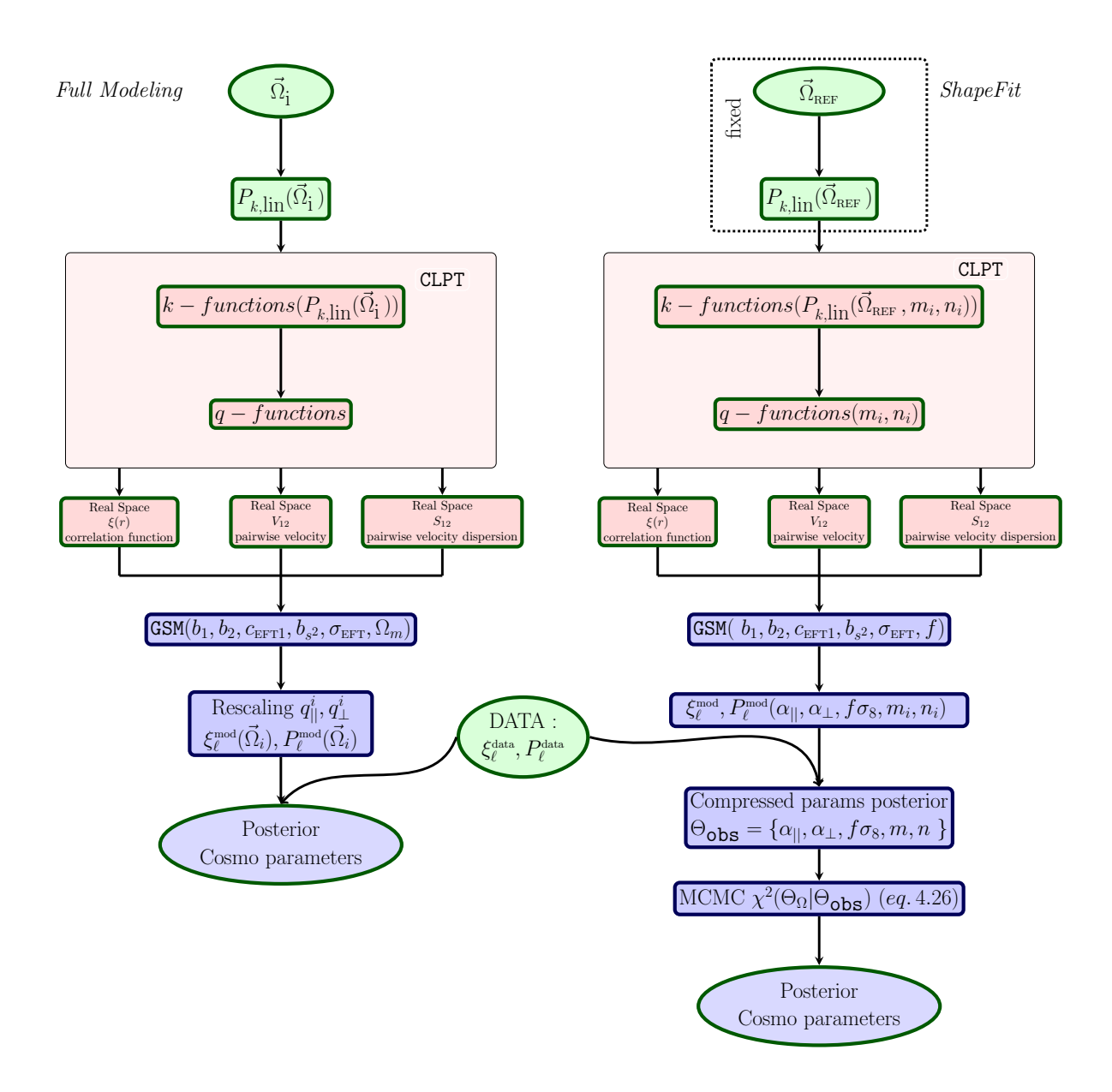


Figure 3. Schemes for the *Full Modeling* (left panel) and the *ShapeFit* (right panel) analysis, allowing to show the differences in the modeling and the cosmological parameters extraction of the information.

$$f = \frac{d\ln D(a)}{d\ln a},\tag{4.2}$$

where D is the growing mode solution. The amplitude of the matter power spectrum fluctuations on scales up to $8 h^{-1}$ Mpc, σ_8 , defined as

$$\sigma_8^2(z) = \int_0^\infty d(\ln k) \, k^3 P(k, z) W_{TH}^2(k \, 8h^{-1} \text{Mpc})$$
 (4.3)

where W_{TH} is a spherical top hat filter. In the standard approach, σ_8 is usually fixed by the reference cosmology and is completely degenerate with f.

The dilation parameters, α 's, are defined as follows:

$$\alpha_{\perp}(z) = \frac{D_A(z) r_{\mathrm{d}}^{\mathrm{ref}}}{D_A^{\mathrm{ref}}(z) r_{\mathrm{d}}}, \quad \alpha_{\parallel}(z) = \frac{H^{\mathrm{ref}}(z) r_{\mathrm{d}}^{\mathrm{ref}}}{H(z) r_{\mathrm{d}}}, \tag{4.4}$$

where D_A denotes the angular diameter distance, H represents the Hubble parameter, and r_d stands for the sound horizon at the drag epoch. The superscript **ref** means that the estimation is conducted within the reference cosmology⁵. In our model, we adopt the alternative parametrization of the distortion parameters:

$$\alpha = \alpha_{\parallel}^{1/3} \alpha_{\perp}^{2/3}, \quad \epsilon = \left(\frac{\alpha_{\parallel}}{\alpha_{\perp}}\right)^{1/3}. \tag{4.5}$$

We incorporate distortions in the clustering by substituting s with $s'(s_{\rm ref}, \mu_{\rm ref})$ and μ with $\mu'(\mu_{\rm ref})$. These substitutions are computed using the re-scaling parameters α and ϵ in the following way:

$$s'(s_{\text{ref}}, \mu_{\text{ref}}) = s_{\text{ref}} \alpha \sqrt{(1+\epsilon)^4 \mu_{\text{ref}}^2 + (1-\mu_{\text{ref}}^2)(1+\epsilon)^{-2}},$$
 (4.6)

$$\mu \ell^2(\mu_{\text{ref}}) = \left[1 + \left(\frac{1}{\mu_{\text{ref}}^2} - 1\right) (1 + \epsilon)^{-6}\right]^{-1}.$$
 (4.7)

The multipoles, denoted as $\xi_{\ell}(s_{\text{ref}})$, are estimated within the reference cosmology using the transformed coordinates $s'(s_{\text{ref}}, \mu_{\text{ref}})$ and $\mu'(\mu_{\text{ref}})$.

To incorporate the dilation parameters into our implementation, we employ interpolation for each modeled multipole, $\xi_{\ell}^{\text{model}}$, utilizing the transformed coordinates $s\prime(s_{\text{ref}},\mu_{\text{ref}})$. Additionally, we calculate the observed Legendre polynomials, $\mathcal{L}^{\text{obs}}(\mu\prime)$, employing the transformed coordinate $\mu\prime(\mu_{\text{ref}})$. We formulate $\xi^{\text{obs}}(s\prime(s_{\text{ref}},\mu_{\text{ref}}),\mu\prime(\mu_{\text{ref}}))$ by combining the product of each multipole and its corresponding Legendre polynomial. The observed multipoles, are expressed as $\xi_{\ell}(s\prime) = \sum_{\ell} a_{\ell\ell\ell} \xi_{\ell\prime}(s)$, where the coefficients $a_{\ell\ell\prime}$ are involved in this summation⁶.

In our *Standard* methodology, we fit the data multipoles to the observed multipoles, and then, we get constraints on the compressed parameters Θ_{obs} and their covariance C_{Θ} . The conversion of compressed parameter constraints into cosmological constraints is done separately and is described in §4.3 below.

4.2 ShapeFit methodology

The *ShapeFit* methodology [94–97] emerges as an extension to the *Standard* methodology, aiming to preserve its agnostic nature while incorporating additional information to enhance its constraining power, thus making it competitive with *Full Modeling*.

This is done by incorporating two additional parameters into the *Standard* methodology variables, compressing the data vector into five parameters $\alpha_{||}$, α_{\perp} , $f\sigma_{s8}$, m, n. The two new parameters affect the slope of the power spectrum, in two different ways: first, an overall re-scaling of the power spectrum slope, through the parameter n, which in principle accounts for a wrong fiducial spectral index n_s ; and second, a scale-dependent slope, through the

 $^{^5}$ Here we refer with reference cosmology as a synonym of fiducial cosmology, we are not distinguishing between grid cosmology or template cosmology.

⁶As shown in previous work [42], an excellent approximation is achieved by truncating the summation at $\ell t = 4$.

parameter m, that models the shape of the power spectrum mainly at wave-numbers around and above the turnaround. This re-scaling process is applied to the template power spectrum P_{ref} to produce a trial spectrum P'_{ref} , defined as follows

$$\ln\left(\frac{P'_{\text{ref}}(k)}{P_{\text{ref}}(k)}\right) = \frac{m}{a} \tanh\left[a \ln\left(\frac{k}{k_p}\right)\right] + n \ln\left(\frac{k}{k_p}\right),\tag{4.8}$$

where the pivot scale $k_p = \pi/r_d$ corresponds to the location where the baryon suppression reaches its maximum.

The two slope re-scaling parameters recover information from the early universe that is imprinted in the broadband shape of the matter power spectrum, this information is omitted in the Standard methodology. In order to extract cosmological information, the slope m is interpreted in terms of the cosmological parameters through [63]

$$m = \frac{d}{d \ln k} \left(\ln \left[\frac{T_{\text{no-wiggle}}^{2} (k_{p}/s, \Theta)}{T_{\text{no-wiggle}}^{2} (k_{p}, \Theta^{\text{ref}})} \right] \right) \Big|_{k=k_{p}}$$

$$= \frac{d}{d \ln k} \left(\ln \left[\frac{P_{\text{no-wiggle}}^{\text{lin}} (k_{p}/s, \Theta)}{P_{\text{no-wiggle}}^{\text{lin}} (k_{p}, \Theta^{\text{ref}})} \frac{P_{\mathcal{R}}(k, \Theta^{\text{ref}})}{P_{\mathcal{R}}(k/s, \Theta)} \right] \right) \Big|_{k=k_{p}}$$

$$(4.9)$$

where $\mathcal{P}_{\mathcal{R}}$ is the primordial power spectrum and T the transfer function. To compute the de-wiggled linear power spectrum, $P_{\text{no-wiggle}}^{\text{lin}}$ we use the Eisenstein-Hu formulae of [98]. In most situations, the parameter n is fixed to zero. However, by letting it free, one can

obtain estimations for n_s through:

$$n = n_s - n_s^{\text{ref}},\tag{4.10}$$

where n_s^{ref} is the spectral index of the reference cosmology.

Another modification to the Standard methodology introduced by ShapeFit involves redefining the amplitude of the clustering. Instead of using the usual σ_8 parameterization, we introduce σ_{s8} as a re-scaling in units of the sound horizon:

$$\sigma_{s8}^{2}(z,\Omega) = \int_{0}^{\inf} d(\ln k) (ks)^{3} P(ks,z) W_{TH}^{2}(ks \, 8h^{-1} \text{Mpc})$$
(4.11)

where $s = r_d/r_d^{\text{ref}}$. By construction, this re-scaling does not vary under the fitting process, and all the compressed variables are expressed in units of the sound horizon.

The templates used in ShapeFit include non-linearities of the power spectrum, which are commonly computed using Eulerian Perturbation Theory. However, to speed up computations, one can use approximations as,

$$P_{22}(k) = \int \frac{d^3p}{(2\pi)^3} P'_{\text{ref}}(p) P'_{\text{ref}}(|\mathbf{k} - \mathbf{p}|) F_2(\mathbf{k}, \mathbf{k} - \mathbf{p})$$
(4.12)

$$\approx \left(\frac{P_{\text{ref}}'(k)}{P_{\text{ref}}(k)}\right)^2 \int \frac{d^3p}{(2\pi)^3} P_{\text{ref}}(p) P_{\text{ref}}(|\boldsymbol{k}-\boldsymbol{p}|) F_2(\boldsymbol{k},\boldsymbol{k}-\boldsymbol{p}), \tag{4.13}$$

Here, $P_{\text{ref}}(p)$ denotes the linear power spectrum of the reference template, while $P'_{\text{ref}}(p)$ represents the linear power spectrum modified by the m ShapeFit parameter. Similarly for the rest of the loop integrals. A validity test of such approximations can be found in [48].

⁷This approximation is important for ShapeFit approach because this computation need to be done at each step of the MCMC chains.

4.2.1 ShapeFit in Configuration Space

As we illustrated in Figure 3, for the computation of the correlation function, we use the GSM presented in §3.1 and the Convolution LPT framework [38] to obtain the necessary ingredients entering eq. (3.8), namely the real space correlation function $\xi(r)$, the pairwise velocity $v_{12}(r)$ and the pairwise velocity dispersion $\sigma_{12}(r)$.

For example, let us consider the simplified version of the one-loop dark matter (unbiased) real space correlation function [38] that is given by

$$1 + \xi(r) = \int \frac{d^3q}{(2\pi)^{3/2} |\mathbf{A}_L|^{1/2}} e^{-\frac{1}{2}(\mathbf{r} - \mathbf{q})^{\mathbf{T}} \mathbf{A}_L^{-1}(\mathbf{r} - \mathbf{q})} \left\{ 1 - \frac{1}{2} A_{ij}^{\text{loop}} G_{ij} + \frac{1}{6} \Gamma_{ijk} W_{ijk} \right\}, \quad (4.14)$$

with q-functions $A_{ij}(\mathbf{q}) = \langle \Delta_i(\mathbf{q})\Delta_j(\mathbf{q})\rangle_c$, and $W_{ijk} = \langle \Delta_i(\mathbf{q})\Delta_j(\mathbf{q})\Delta_k(\mathbf{q})\rangle_c$, where $\Delta_i = \Psi_i(\mathbf{q}) - \Psi_i(0)$. In the case of matrix **A**, which is split into linear and loop pieces

$$A_{ij}(\mathbf{q}) = 2 \int \frac{d^3k}{(2\pi)^3} \left(1 - e^{i\mathbf{p}\cdot\mathbf{q}}\right) \frac{k_i k_j}{k^4} \left(P_L(k) + \frac{3}{7} Q_1(k) + \frac{10}{21} R_1(k)\right)$$

$$= A_{ij}^L(\mathbf{q}) + A_{ij}^{\text{loop}}(\mathbf{q}), \tag{4.15}$$

where the k-functions $Q_1(k)$ and $R_1(k)$ are functions constructed out of four-point functions of linear density fields, defined in [37] as,

$$Q_1(k) = \int \frac{d^3p}{(2\pi)^3} q_1(\boldsymbol{k}, \boldsymbol{p}) P_L(p) P_L(|\boldsymbol{k} - \boldsymbol{p}|), \tag{4.16}$$

$$R_1(k) = \int \frac{d^3p}{(2\pi)^3} r_1(\mathbf{k}, \mathbf{p}) P_L(k) P_L(p), \qquad (4.17)$$

for kernels q_1 and r_1 . In *ShapeFit* we produce the trial matrix AI_{ij} , by substituting the trial power spectrum PI_{ref} of eq. (4.8) into eq. (4.15). To speed up the computations, as it is done in the case of the non-linear power spectrum, we evaluate functions Q_1 and R_1 as

$$Q_1(k; m, n) = \left(\frac{P'_{\text{ref}}(k; m, n)}{P_{\text{ref}}(k)}\right)^2 \int \frac{d^3p}{(2\pi)^3} q_1(\boldsymbol{k}, \boldsymbol{p}) P_{\text{ref}}(p) P_{\text{ref}}(|\boldsymbol{k} - \boldsymbol{p}|), \tag{4.18}$$

$$R_1(k; m, n) = \left(\frac{P'_{\text{ref}}(k; m, n)}{P_{\text{ref}}(k)}\right)^2 \int \frac{d^3p}{(2\pi)^3} r_1(\mathbf{k}, \mathbf{p}) P_{\text{ref}}(k) P_{\text{ref}}(p), \tag{4.19}$$

where we have written explicitly the dependence of the trial functions on the *ShapeFit* parameters.

This method is analogously applied for all k-functions, from which the q-functions are constructed, and finally for the real space correlation function $\xi(r)$, the pairwise velocity $v_{12}(r)$, and velocity dispersion $\sigma_{12}(r)$, which are necessary to construct the redshift space GSM correlation function.

These ingredients are computed for biased tracers using CLPT, obtaining, The real space correlation function $\xi_X(r)$, which corresponds to the zeroth-order moment for tracer X, is

obtained within CLPT, [35, 37, 38, 40, 80, 82],

$$1 + \xi_{X}(r) = \int \frac{d^{3}q}{(2\pi)^{3/2} |\mathbf{A}_{L}|^{1/2}} e^{-\frac{1}{2}(\mathbf{r} - \mathbf{q})^{\mathbf{T}} \mathbf{A}_{L}^{-1}(\mathbf{r} - \mathbf{q})} \left\{ 1 - \frac{1}{2} A_{ij}^{loop} G_{ij} + \frac{1}{6} \Gamma_{ijk} W_{ijk} + b_{1}(-2U_{i}g_{i} - A_{ij}^{10}G_{ij}) + b_{1}^{2}(\xi_{L} - U_{i}U_{j}G_{ij} - U_{i}^{11}g_{i}) + b_{2}(\frac{1}{2}\xi_{L}^{2} - U_{i}^{20}g_{i} - U_{i}U_{j}G_{ij}) - 2b_{1}b_{2}\xi_{L}U_{i}g_{i} - 2b_{s^{2}}g_{i}V_{i}^{10} + b_{s^{2}}^{2}\zeta - 2b_{1}b_{s^{2}}g_{i}V_{i}^{12} + b_{2}b_{s^{2}}\chi^{12} - \frac{1}{2}c_{1,\text{EFT}} \operatorname{tr} G \right\},$$

$$(4.20)$$

for bias parameters b_1 , b_2 and b_{s^2} and EFT counterterm $c_{1,\rm EFT}$. The linear correlation function is

$$\xi_L(q) = \int \frac{d^3p}{(2\pi)^3} e^{i\mathbf{p}\cdot\mathbf{q}} P_L(p), \tag{4.21}$$

and we used the functions

$$A_{ij}^{mn} = \langle \delta^m(\mathbf{q})\delta^n(0)\Delta_i \Delta_i \rangle_c, \qquad U_i^{mn} = \langle \delta^m(\mathbf{q})\delta^n(0)\Delta_i \rangle_c. \tag{4.22}$$

The involved r and q dependent tensors are $g_i = (\mathbf{A}_L^{-1})_{ij}(r_j - q_j)$, $G_{ij} = (\mathbf{A}_L^{-1})_{ij} - g_i g_j$, and $\Gamma_{ijk} = (\mathbf{A}_L^{-1})_{\{ij} g_{k\}} - g_i g_j g_k$.

The pairwise velocity is given by

$$v_{12}(\mathbf{r}) = \frac{f\,\hat{r}_{i}}{1 + \xi_{X}(r)} \int \frac{d^{3}q\,e^{-\frac{1}{2}(\mathbf{r}-\mathbf{q})^{T}\mathbf{A}_{L}^{-1}(\mathbf{r}-\mathbf{q})}}{(2\pi)^{3/2}|\mathbf{A}_{L}|^{1/2}} \left\{ -g_{r}\dot{A}_{ri} - \frac{1}{2}G_{rs}\dot{W}_{rsi} + b_{1}\left(2\dot{U}_{i} - 2g_{r}\dot{A}_{ri}^{10} - 2G_{rs}U_{r}\dot{A}_{si}\right) + b_{1}^{2}\left(\dot{U}_{i}^{11} - 2g_{r}U_{r}\dot{U}_{i} - g_{r}\dot{A}_{ri}\xi_{L}\right) + b_{2}\left(\dot{U}_{i}^{20} - 2g_{r}U_{r}\dot{U}_{i}\right) + 2b_{1}b_{2}\xi_{L}\dot{U}_{i} \right\},$$

$$(4.23)$$

and the pairwise velocity dispersion

$$\sigma_{12}^{2}(\mathbf{r}) = \frac{f^{2} \hat{r}_{i} \hat{r}_{j}}{1 + \xi_{X}(r)} \int \frac{d^{3}q \, e^{-\frac{1}{2}(\mathbf{r} - \mathbf{q})^{T} \mathbf{A}_{L}^{-1}(\mathbf{r} - \mathbf{q})}}{(2\pi)^{3/2} |\mathbf{A}_{L}|^{1/2}} \left\{ \ddot{A}_{ij} - g_{r} \ddot{W}_{rij} - G_{rs} \dot{A}_{ri} \dot{A}_{sj} + 2b_{1} \left(\ddot{A}_{ij}^{10} - g_{r} \dot{A}_{r\{i} \dot{U}_{j\}} - g_{r} U_{r} \ddot{A}_{ij} \right) + b_{1}^{2} \left(\xi_{L} \ddot{A}_{ij} + 2\dot{U}_{i} \dot{U}_{j} \right) + 2b_{2} \dot{U}_{i} \dot{U}_{j} \right\},$$
(4.24)

with q-coordinate dependent correlators

$$\dot{A}_{ij}^{mn}(\mathbf{q}) = \frac{1}{fH} \langle \delta_1^m \delta_2^n \Delta_i \dot{\Delta}_j \rangle, \qquad \ddot{A}_{ij}^{mn}(\mathbf{q}) = \frac{1}{f^2 H^2} \langle \delta_1^m \delta_2^n \dot{\Delta}_i \dot{\Delta}_j \rangle,
\dot{W}_{ijk} = \frac{1}{fH} \langle \Delta_i \Delta_j \dot{\Delta}_k \rangle, \qquad \ddot{W}_{ijk} = \frac{1}{f^2 H^2} \langle \Delta_i \dot{\Delta}_j \dot{\Delta}_k \rangle,
\dot{U}^{mn}(\mathbf{q}) = \frac{1}{fH} \langle \delta_1^m \delta_2^n \dot{\Delta}_i \rangle, \tag{4.25}$$

where $\dot{A}_{ij} \equiv \dot{A}_{ij}^{00}$ and $\ddot{A}_{ij} \equiv \ddot{A}_{ij}^{00}$.

Finally, we would like to highlight that our EFT model is not exhaustive, as it does not encompass all PT corrections and counterterms up to 1-loop. Nonetheless, we adopt this simplified approach for two main reasons: firstly, it has been extensively validated in prior research [79]; and secondly, we demonstrate in this work that it satisfactorily meets the requirements of DESI Y1 data. Nevertheless, complete LPT/EFT frameworks are available in the literature [99, 100].

4.3 Inferring cosmological parameters from compressed parameters

As depicted in the bottom row of the schematic in the right panel of Figure 3, our compressed methodology incorporates an additional step to derive cosmological parameters from our final compressed parameters. In this section, we briefly summarize the methodology employed to achieve this.

Let Θ_{obs} represent our final set of compressed parameters. We aim to use them to determine a set of cosmological parameters $\Omega = \{\omega_m, A_s, h, ...\}$. For a given value of these parameters we can compute a set of compressed parameters Θ_{Ω} from theory following the equations presented in sections 4.1 and 4.2. We use these equations to run an MCMC chain that finds the regions of the parameter space of Ω for which Θ_{Ω} is a good fit of Θ_{obs} . Let C_{Θ} be the covariance of a given compressed parameter, and then if we assume a Gaussian likelihood⁸ for our MCMC exploration, the χ^2 is defined as:

$$\chi^2(\Theta_{\Omega} - \Theta_{\text{obs}}) = (\Theta_{\Omega} - \Theta_{\text{obs}})^T C_{\Theta}^{-1}(\Theta_{\Omega} - \Theta_{\text{obs}}), \tag{4.26}$$

As mentioned earlier, we employ two compression methodologies, namely the *Standard* and *Shape-fit* methods. In our *Standard* approach, Θ_{Ω} is as follows:

$$\Theta_{\Omega} = \{ D_A(z, \Omega) / r_d(\Omega), D_H(z) / r_d(\Omega), f\sigma_8(z, \Omega) \}$$
(4.27)

where the equations used for computing the compressed variables are 4.5, 4.2 and 4.3, and we have explicitly included their dependence on the cosmological models into our notation.

Within our *Shape-Fit* methodology, in addition to the equations of the *Standard* approach, we also need to consider the equations for the additional parameters n and m, thus Θ_{Ω} are given by:

$$\Theta_{\Omega} = \{ D_A(z, \Omega) / r_d(\Omega), D_H(z) / r_d(\Omega), f_{\sigma_{s8}}(z, \Omega), m(\Omega), n(\Omega) \}, \tag{4.28}$$

where m, n, and σ_{s8} are respectively given by equations 4.9, 4.10, and 4.11.

Also in the case of *ShapeFit*, we have to keep in mind that the m parameter changes the tilt and the amplitude of the power spectrum, which means that we are varying σ_{s8} . This deformation of the power spectrum is captured through [63]:

⁸A Gaussian likelihood is a good approximation when the distributions of Θ_{obs} are gaussian distributed, what can be verified in the posteriors of the compressed parameters

$$f\sigma_{s8} = f \frac{(f\sigma_{s8})^{\text{ref}}}{\left(f\left(P_{\text{lin}}\left(k_{p}\right)\right)^{1/2}\right)^{\text{ref}}} \left(\frac{1}{s^{3}}P_{\text{lin}}\left(k_{p}/s\right)\right)^{1/2}$$

$$= \frac{(f\sigma_{s8})^{\text{ref}}}{\left(fA_{sp}^{1/2}\right)^{\text{ref}}} (fA_{sp}^{1/2}) \times \exp\left(\frac{m}{2a}\tanh\left(a\ln\left(\frac{r_{d}^{\text{ref}}}{8}\right)\right)\right)$$

$$\approx \frac{(fA_{sp}^{1/2})}{\left(fA_{sp}^{1/2}\right)^{\text{ref}}} (f\sigma_{s8})^{\text{ref}}$$

$$(4.29)$$

where

$$A_{sp} = s^{-3} P_{\text{no-wiggle}}^{\text{lin}} \left(k_p / s, \mathbf{\Theta} \right), \tag{4.30}$$

with Θ the cosmological parameters of the cosmology of reference or the new one. The last step of equation 4.29 can be done thanks to the fact that we only use the amplitude at the pivot scale during the MCMC exploration.

4.4 Full Modeling in Configuration space

In the Full Modeling approach, which is illustrated in the left side of Figure 3, we use a non-fixed template, which consists of modifying the shape of the linear power spectrum through the variation of the cosmological parameters $\omega_{\rm cdm}$, ω_b , h, A_s , n_s , $N_{\rm eff}$, $\Omega_{\rm ncdm}$, parameters that also depends on early-time physics, in contrast to the Standard approach. This methodology involves using a Boltzmann solver code like CLASS or CAMB, and, computing the 1-loop corrections for the perturbative approach used, in each step of the MCMC exploration. Despite its higher computational cost, this allows us to extract cosmological information not only from late-time physics but also from early-time physics (in contrast with Standard methodology). Hence, the Full Modeling approach, at least in principle, can impose tighter constraints than the Standard methodology as it captures more information. As mentioned previously, Shapefit also looks for extract additional information from early-time physics through the additional parameters.

However, the high dimensionality of the parameter space requires the use of new tools to speed up the template generation. In [42], we presented a neural network approach that enhanced the efficiency of convergence time during MCMC exploration dramatically. As clustering measurements employ a cosmology of reference to transform redshift into distance measurements, we need to add two distortion parameters that compensate the Alcock-Paczynski effect, denoted them as $q_{||}$ and q_{\perp} , and following a similar description of 4.1 with the difference that we do not introduce the BAO scale at the drag epoch, $r_{\rm d}$, as its effect is already included in the variation of the linear power spectrum.

The geometric distortion parameters, perpendicular, and parallel to the line of sight, in the *Full Modeling* approach are defined as

$$q_{\perp}(z) = \frac{D_A(z)}{D_A^{\text{ref}}(z)}, \quad q_{\parallel}(z) = \frac{H^{\text{ref}}(z)}{H(z)},$$
 (4.31)

here D_A is the angular diameter distance, H is the Hubble parameter, and the ref superscript indicates that the estimate is done in the reference or fiducial cosmology of the data multipoles.

The *Full Modeling* methodology offers the advantage of capturing a broad range of dynamic-times, as it does not need to fix the early-time dynamics of the universe. However, it requires the adoption of a specific cosmological model, and for exploring alternative models of interest, a complete rerun of the MCMC is needed.

In Table 1 we show the varied parameters and their priors for our baseline Full Modeling analyses. We keep fixed the slope $n_s = 0.97$, the effective number of relativistic degrees of freedom $N_{\rm eff} = 3.046$, the massive neutrino abundance $\omega_{\rm ncdm} = 0.00064$ and we impose a big-bang nucleosynthesis (BBN) prior $\mathcal{N}[\mu = 0.02237, \sigma = 0.00037]$ to ω_b [101].

4.5 GSM-EFT code for compressed and direct fits: Users guide

We present our GSM-EFT C-code that computes the multipoles of the one-loop GSM two-point correlation function in redshift space⁹. The GSM-EFT code receives as an input, the linear power spectrum, obtained from a Boltzmann Solver like CAMB or CLASS, as well as a set of nuisance parameters: including biases $\{b_1, b_2, b_{s^2}\}$, the EFT parameters $\{\sigma_{\rm EFT}^2, c_1^{\rm EFT}\}$ and the cosmological parameter Ω_m^{10} . The code produces as GSM-EFT outputs the correlation function multipoles $\ell=0,2,4$ in redshift space.

- GSM-CosmoExtractor. The repository includes a python wrapper and has two distinct approaches implemented for extracting the cosmological information explored in this work (developed in section 4). The wrapper also includes a function to compute the CAMB/CLASS linear power spectrum required as an input by our GSM-EFT code. The methodology for modeling the effects of the re-scaling parameters $\{\alpha_{||}, \alpha_{\perp}\}$ (Eqs. 4.4) required for compressed parameters, as well as the re-scaling parameters in Full Modeling, the $\{q_{||}, q_{\perp}\}$ are also implemented in the python wrapper.
- GSM-EFT modules The GSM-EFT code is composed of two separate modules: CLPT and GSM. The CLPT module computes the real-space correlation function, pairwise velocity, and velocity dispersion. Then, the GSM module receives the CLPT output statistics as inputs along with values of the nuisance parameters (bias and EFT terms), and outputs the redshift-space two-point correlation function. In Section 4.2.1 below, we describe the implementation of the compressed approaches in the wrapper as well as in the GSM-EFT code. The GSM-EFT code takes only ~ 1 second in computing the redshift multipoles, using either the Full Modeling or ShapeFit approaches. While this is a relatively small time, given the sheer number of evaluations required for our MCMC analysis and the large number of analyses we require, there is an incentive to accelerate the model evaluation time even further. As introduced in section 3.2, we generated an emulator to reduce the processing time to around 0.015 seconds per evaluation.
- ShapeFit implementation in GSM-EFT. As indicated in Figure 3, the implementation of ShapeFit in GSM-EFT code implies a modification of the CLPT module. This is done through two modifications to the original pipeline: First, the k-funtions that depend on the $P_L(k)$ and loop corrections, are pre-computed using the modified linear power spectrum $P_{ref}(k)$. Then, the q-functions are computed from k-functions, this is done trough the re-scaling factor $\left(\frac{P'_{ref}(k)}{P_{ref}(k)}\right)^2$.

⁹https://github.com/alejandroaviles/gsm.

 $^{^{10}\}Omega_m$ is necessary to calculate the growth rate f at the output redshift

Free parameters and priors					
Cosmological		Compressed			
h	$\mathcal{U}[0.55, 0.91]$	$f\sigma_8$	$\mathcal{U}[0,1]$		
ω_b	$\mathcal{N}[0.02237, 0.00037]$	$lpha_{\perp}$	$\mathcal{U}[0.5, 1.5]$		
$\omega_{ m cdm}$	$\mathcal{U}[0.08,0.16]$	$lpha_\parallel$	$\mathcal{U}[0.5, 1.5]$		
$\log(10^{10}A_s)$	$\mathcal{U}[2.0, 4.0]$	m	$\mathcal{U}[-1,1]$		
	Nuisances				
b_1	$\mathcal{U}[0, 2.0]$	b_2	$\mathcal{U}[-5, 10]$		
$\sigma_{ m EFT}^2$	$\mathcal{U}[-20, 100]$	$c_{1,\mathrm{EFT}}$	$\mathcal{U}[-100, 100]$		
b_{s^2}	$\mathcal{U}[-10,10]$				

Table 1. Free parameters and priors we use for the baseline Full Modeling analyses of ABACUS-SUMMIT simulations. The nuisance parameters with their priors are the same for all three methods. We fix the spectral index of the power spectrum to the Planck 2019 value $n_s = 0.9649$.

4.6 Likelihood and Priors

Our exploration of the parameter space is done through the Bayes law, with the Bayesian evidence neglected. For a given model, the posterior probability of a point in the parameter space, denoted as $\mathcal{P}(\theta)$, is defined as follows:

$$\mathcal{P}(\boldsymbol{\theta} \mid \boldsymbol{D}) \propto \mathcal{L}(\boldsymbol{D} \mid \boldsymbol{\theta}) \times \pi(\boldsymbol{\theta}),$$
 (4.32)

where, $\mathcal{L}(D \mid \theta)$ is the likelihood and $\pi(\theta)$ is the prior distributions. If we assume that the parameter space follows a normal distribution, we can express the likelihood as,

$$\mathcal{P}(\boldsymbol{D} \mid \boldsymbol{\theta}) \propto (\chi^2)^{\frac{\nu-2}{2}} \exp\left(-\frac{\chi^2}{2}\right),$$
 (4.33)

where ν is the number of degrees of freedom, and χ^2 is defined as $\chi^2 = (\boldsymbol{m} - \boldsymbol{d})^T C^{-1} (\boldsymbol{m} - \boldsymbol{d})$, and the vectors \boldsymbol{m} and \boldsymbol{d} represent the model and data respectively. The covariance matrix of the data is denoted as C.

The exploration of parameter space is done using the publicly available MCMC code emcee [102] which is an ensemble sampler with affine invariance defined in [103]. This code has some advantages, like enabling parallelization, allowing us to take advantage of the computational power of large clusters. In our work, we employ the priors outlined in Table 1 for all of our three independent methodologies. In all the cases we fix the spectral index $n_s = 0.97$ unless stated otherwise, the effective number of relativistic degrees of freedom $N_{\rm eff} = 3.046$, and the massive neutrino abundance $\omega_{\rm ncdm} = 0.00064$.

To guarantee convergence, we employ an integrated auto-correlation time, which is monitored every 100 steps [103]. Convergence is considered achieved when two conditions are simultaneously satisfied: the chain's length surpasses 100 times the estimated auto-correlation time, and the alteration in this estimation remains below 1%.

5 Cosmological constraints from configuration-space clustering statistics

In this section, we discuss and compare the results obtained with our pipeline following three different methodologies: Standard, ShapeFit, and $Full\ Modeling$. However, our attention will primarily be on ShapeFit and $Full\ Modeling$, given their stronger constraining potential. In Section 5.1, we explore the settings for defining our baseline analysis, in particular the range of the fits, and the bias settings. In the Section 5.2, we explore extensions to the baseline analysis, as including the hexadecapole, the extension of the parameter space including n_s and the $\omega_0 - \omega_a$. Section 5.3 is devoted to exploring the performance of the analysis for the different DESI tracers and their combination of them. Finally, in the last section, we compare the constraining power of the two methodologies, ShapeFit, and $Full\ Modeling$, in the cosmological parameter space.

5.1 Baseline Analysis

We start by exploring the behavior of the GSM model for different volumes with Full Modeling and Shape Fit. Figure 4 shows the posteriors for the LRG tracer with a minimal scale of $s_m in = 30 h^{-1}$ Gpc for three different volumes: $8 h^{-3}$ Gpc³, which represents approximately the volume for DESI first year, $40 h^{-3} \,\mathrm{Gpc}^3$ which represents the volume of DESI by the end of the fifth year, and $200 h^{-3}$ Gpc³ with the total combined volume of the 25 simulations and which represents an unrealistic volume for a survey but allows us to test models with very small error bars. In Table 2 we report the central values and 1σ errors for the cosmological parameters. As expected, when we extend to larger volumes, our constraints become tighter, maintaining approximately the same central values of the posteriors. In Full Modeling all our constraints tend to fall within the range of 1σ for h (0.42 σ for V_1 , 0.61 σ for V_5 and 1.14 σ for V_{25}) and within the range of $1-2\sigma$ for $\ln(10^{10}A_s)$ (0.46 σ for V_1 , 0.11 σ for V_5 and 1.4 σ for V_{25}), while Ω_m consistently remains below 1σ (0.05 σ for V_1 , 0.12 σ for V_5 and 0.28 σ for V_{25}). On the other hand, in Shape Fit, we obtain constraints within the range of $1-2\sigma$ $f\sigma_8$ (0.04 σ for V_1 , 0.50σ for V_5 and 1.7σ for V_{25}) and below 1σ for α_{\parallel} (0.28 σ for V_1 , 0.48 σ for V_5 and 0.94σ for V_{25}), while α_{\perp} remains around $1-2\sigma$ (0.44 σ for V_1 , 0.97 σ for V_5 and 2.42 σ for V_{25}) and lastly, for m we obtain constrains around 1σ (0.03 σ for V_1 , 0.41 σ for V_5 and 1.14 σ for V_{25}).

The increasing shift for the largest volume can be understood by considering the limitations of our 1-loop corrections, however even for the largest volume we do not detect a significant shift in any parameter. Considering the limitations in accuracy of N-body simulations that we start being sensitive to at these big volumes [e.g. 104], whose systematics potentially could be indistinguishable from inaccuracies in the modeling, and given the interest of comparing the errors with the current DESI year one analysis, we decided throughout the rest of this work, to report the results for a volume of $8 h^{-3} \,\mathrm{Gpc}^3$ (unless otherwise stated).

5.1.1 Optimizing the fitting range

In what follows, we present the results of our fits to the mean of the 25 ABACUS-SUMMIT simulations, employing the methodologies detailed in section 4. We define our baseline methodology as using the monopole and quadrupole of the correlation function, using the covariance for a volume of $8 h^{-3} \,\mathrm{Gpc}^3$, with a maximum scale of $s_{max} = 130 h^{-1} \,\mathrm{Mpc}$ for the three methodologies. For the tests of the baseline settings, we focus on the LRG sample. We explore

,						
Full Modeling						
Volume	Ω_m	h	$\ln(10^{10}A_s)$			
$V_1 = 8h^{-3}\mathrm{Mpc}^3$	0.3147 ± 0.0099	0.6771 ± 0.0083	2.98 ± 0.12			
$V_5 = 40h^{-3}\mathrm{Mpc^3}$	0.3146 ± 0.0046	0.6768 ± 0.0052	3.003 ± 0.058			
$V_{25} = 200h^{-3}{\rm Mpc}^3$	0.3146 ± 0.0021	0.6776 ± 0.0035	2.999 ± 0.026			
		Shape Fit				
Volume	$f\sigma_8$	$lpha_\parallel$	$lpha_{\perp}$	m		
$V_1 = 8h^{-3}\mathrm{Mpc^3}$	0.449 ± 0.025	1.005 ± 0.018	0.9965 ± 0.0079	-0.001 ± 0.031		
$V_5 = 40h^{-3}\mathrm{Mpc}^3$	0.444 ± 0.012	1.0037 ± 0.0077	$0.9960^{+0.0039}_{-0.0043}$	0.007 ± 0.017		
$V_{25} = 200h^{-3}\mathrm{Mpc}^3$	0.4408 ± 0.0054	1.0033 ± 0.0035	0.9954 ± 0.0019	$0.0107^{+0.0088}_{-0.0099}$		

Table 2. Summary of the constraints obtained when fitting the ABACUS LRG sample with our *Full Modeling* and *Shape Fit* methodology for $s_{\min} = 30h^{-1}{\rm Mpc}$ using different volumes.

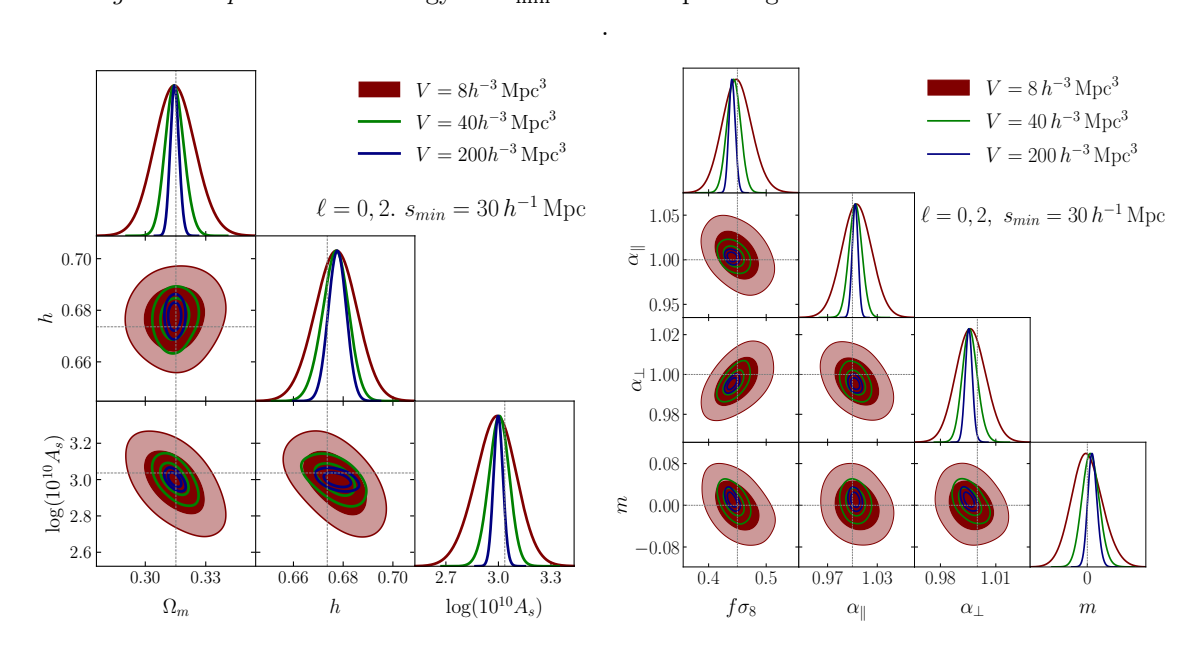


Figure 4. The triangular plot shows the posterior distribution of our EFT-GSM templates from section 3, obtained when we fit the mean of 25 ABACUS-SUMMIT simulations using a different rescaling number for the covariance matrix. On the left, we have the fit resulting from *Full-Modeling*, while on the right, we have the *Shape Fit*. The non-rescaled covariance matrix is in maroon, the covariance matrix rescaled by 5 in green, and the covariance matrix rescaled by 25 in blue. All the plots are obtained for the LRG tracer with $s_{min} = 30h^{-1}\text{Gpc}$.

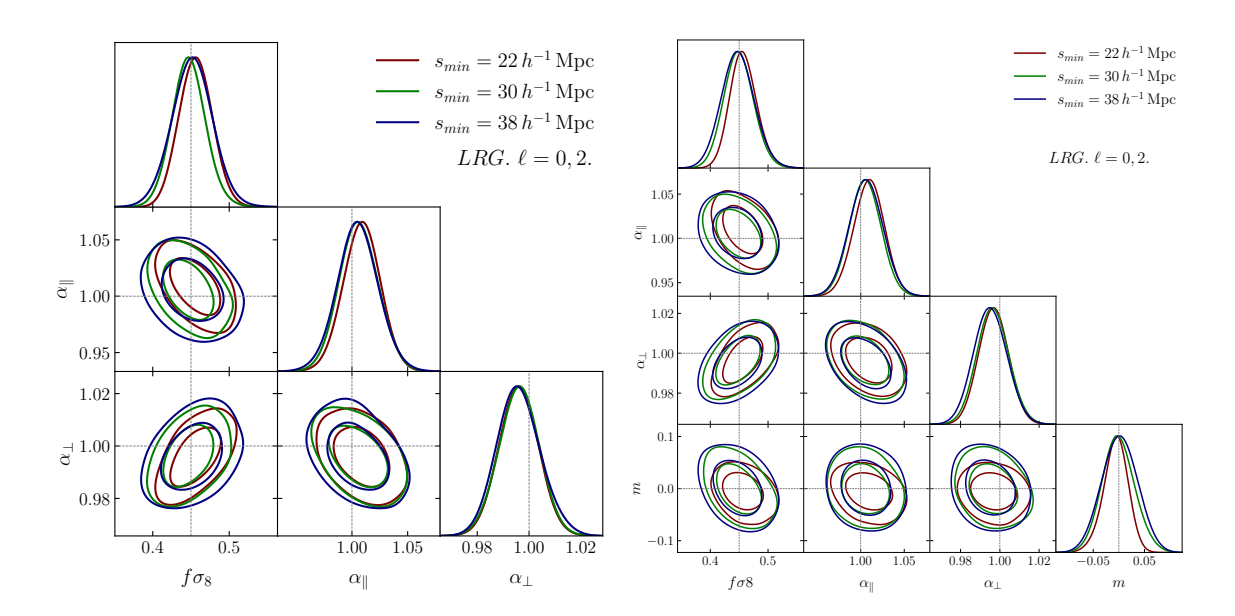


Figure 5. The triangular plot shows the posterior distribution obtained from the mean of 25 ABACUS-SUMMIT simulations using a non-rescaled covariance matrix for the LRG tracer. On the left side, we have constraints for the *Standard* methodology, while on the right side, we have constraints for the *ShapeFit* methodology. We plot three different ranges for the LRG tracers, a minimum scale $s_{min} = 22 \, h^{-1} {\rm Mpc}$ in red, $s_{min} = 30 \, h^{-1} {\rm Mpc}$ in green, and $s_{min} = 38 \, h^{-1} {\rm Mpc}$ in blue.

in this section the performance of the GSM-EFT model for different minimum scales for all methodologies *Standard* analysis, *ShapeFit* and *Full Modeling*.

In the Standard analysis, we constrain $f\sigma_8$, α_\perp and α_\parallel parameters, introduced in the section 4.1, and, given that the reference template is computed based on the ABACUS-SUMMIT cosmology, we expect $\alpha_\perp=1$ and $\alpha_\parallel=1$. In the ShapeFit methodology, we also include the m parameter, which, we expect to be 0. In Figure 5 we show the constraints for both methodologies in our baseline analysis. We compare the results of the Standard methodology (left) and of the ShapeFit (right) for three different minimum scale s_{min} equal to: $22\,h^{-1}$ Mpc, $30\,h^{-1}$ Mpc, and $38\,h^{-1}$ Mpc. In Table 3 we present the quantitative results. We observe that all the results are in agreement with the cosmology of the ABACUS-SUMMIT within 1σ . We observe a similar performance among these two methodologies for the parameters in common, which is something we expect, given the parameter m is intended to provide independent information. This is the extra information that m captures about the slope of the linear power spectrum, which makes ShapeFit as constraining as Full-Modeling when interpreting the set of compressed parameters from ShapeFit into the cosmological parameters of Λ CDM, as shown in [94, 95].

In Full Modeling we define as our baseline analysis, four free cosmological parameters, $\{\Omega_m, h, \ln(10^{10}A_s), \omega_b\}$, however as we explained in the methodology we impose a Gaussian BBN prior on ω_b , as well as flat priors in the nuisance parameters which are described in Table 1. In Figure 7 we plot the posterior distribution contours for our baseline analysis varying s_{min} for three different values with a bin separation of $8 h^{-1}$ Mpc, on the right side we have a triangular plot for the Full Modeling methodology while on the left side, we have the ShapeFit methodology. We show the values in Table 4. We notice that both methodologies are in good

Baseline

ShapeFit for Maximal Freedom						
$s_{ m min}$ $f\sigma_8$ $lpha_\parallel$ $lpha_\perp$						
$22 h^{-1}{ m Mpc}$	$0.457^{+0.021}_{-0.025}$	1.010 ± 0.017	0.9968 ± 0.0074	$-0.006^{+0.025}_{-0.022}$		
$30 h^{-1}{ m Mpc}$	0.449 ± 0.025	1.005 ± 0.018	0.9965 ± 0.0079	-0.001 ± 0.031		
$38h^{-1}{\rm Mpc}$	0.448 ± 0.028	1.006 ± 0.019	0.9951 ± 0.0083	0.002 ± 0.034		
	Stan	dard for Maxim	al Freedom			
$22 h^{-1}{\rm Mpc}$	0.456 ± 0.021	1.009 ± 0.016	0.9960 ± 0.0074	-		
$30 h^{-1}{ m Mpc}$	0.447 ± 0.022	1.006 ± 0.017	0.9961 ± 0.0076	-		
$38 h^{-1} \mathrm{Mpc}$	0.452 ± 0.026	1.005 ± 0.018	$0.9960^{+0.0079}_{-0.0087}$	-		

Table 3. Constraints on our compressed parameters when fitting our ABACUS LRG sample for three minimum scales when using *Standard* and *ShapeFit* methodology.

agreement with the true values of the cosmological parameters for all scales, within $\leq 0.1\sigma$ for Ω_m , $\leq 0.6\sigma$ for h and, $\leq 0.7\sigma$ for A_s when $s_{min} = 22\,h^{-1}{\rm Mpc}$ for Full modeling and ShapeFit. For ShapeFit we observe a similar trend, all deviations from the true value are $\leq 0.2\sigma$ for Ω_m , $\leq 0.4\sigma$ for h and $\leq 0.5\sigma$ for $\ln(10^{10}A_s)$. We conclude, we do not detect any significant shift with either of the methodologies employed. In Figure 6, we illustrate the shape of the correlation function. This depiction represents the mean of the values derived from the fit of the baseline analysis, with $s_{min} = 30, h^{-1}{\rm Mpc}$, and a $\chi^2 = 60.57$ for 58 bins and 9 free parameter.

As we can notice from the results in this section, although we obtain results below 1σ for all the choices of minimum scales, the results with $s_{min} = 22 \, h^{-1} \rm Mpc$ provide the smallest error bars without any detectable bias, which is in agreement with what other works have concluded [42]. Therefore, our optimal fitting range is $s_{\rm range} = 22 - 130 \, h^{-1} \rm Mpc$. Several crucial results will be exclusively presented with this range, unless otherwise specified. Our baseline analysis is extended and compared in further sections.

5.1.2 Maximal and minimal freedom

We explore two different parameter space configurations of the galaxy bias terms, that we refer to as maximal and minimal freedom. In the first, we let all parameters vary simultaneously and it is considered as our baseline configuration. While the second configuration assumes a co-evolution for which non-local biases appear only through gravity evolution, and so are not present in Lagrangian coordinates scheme, corresponding to fix $b_{s^2} = 0$.

Figure 8 shows the mean value of the posterior distribution of the parameters found when running our methodology using both *maximal* and *minimal* freedom configurations and using both *ShapeFit* and *Full Modeling* methods. The corresponding quantitative results are presented in Tables 3, 4, 5 and 6. We notice that in both our it Full Modeling and

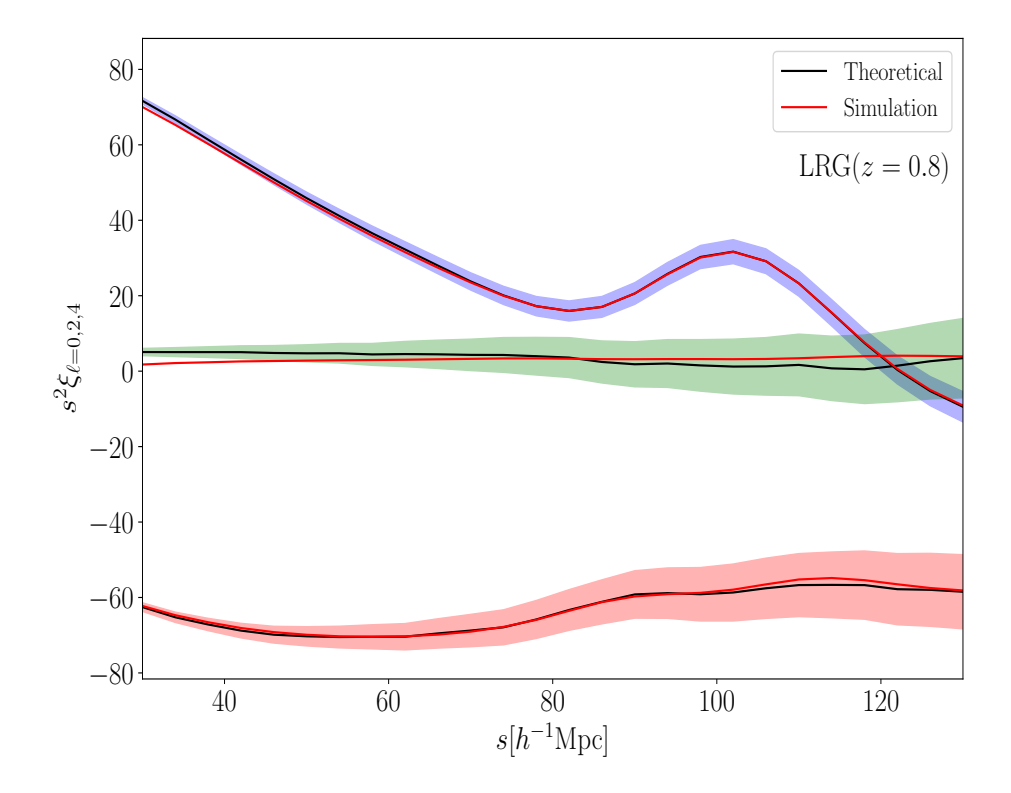


Figure 6. This plot shows the correlation function obtained from the mean of 25 ABACUS-SUMMIT simulations and the mean of the posterior distribution in the range $s_{min} = 30 \, h^{-1} \text{Mpc}$ and $s_{max} = 130 \, h^{-1} \text{Mpc}$. The shadow regions show the error bars from the non-rescaled covariance matrix for the LRG tracer.

it Shape Fit results, the central values are fairly consistent with each other. However, the *Minimal* freedom configuration leads to $\sim 10\%$ smaller error bars, this trend is expected as we reduce the number of free parameters. We notice that the it Full Modeling scenario shows an underestimation of the A_s parameters in this larger scale which is closer to its expected value at $22\,h^{-1}{\rm Mpc}$.

On the other hand, if we explore the compressed parameter space for the $22h^{-1}{\rm Mpc}$ scale specifically, we observe that the *Maximal* freedom mean value predictions are closer to the true value of the simulation for $f\sigma_8$, while the *Minimal* freedom case fares better with its predictions for α_{\parallel} . Additionally, we show that the error bars are of similar size for all parameters except m, where the *Maximal* freedom case leads to tighter constraints.

In conclusion, our comparison between the predicted central values and the expected values of our parameters reveals similar performances between our *Minimal* and *Maximal* freedom configurations. This holds true for both the compressed parameter space and the cosmological parameter space. We observe no significant shift of the fitted parameters from their true value. However, our baseline analysis with $s_{min} = 22 \, h^{-1} \rm Mpc$ indicates a improvement in most parameters of approximately $\sim 10\%$ in the size of the error bars when

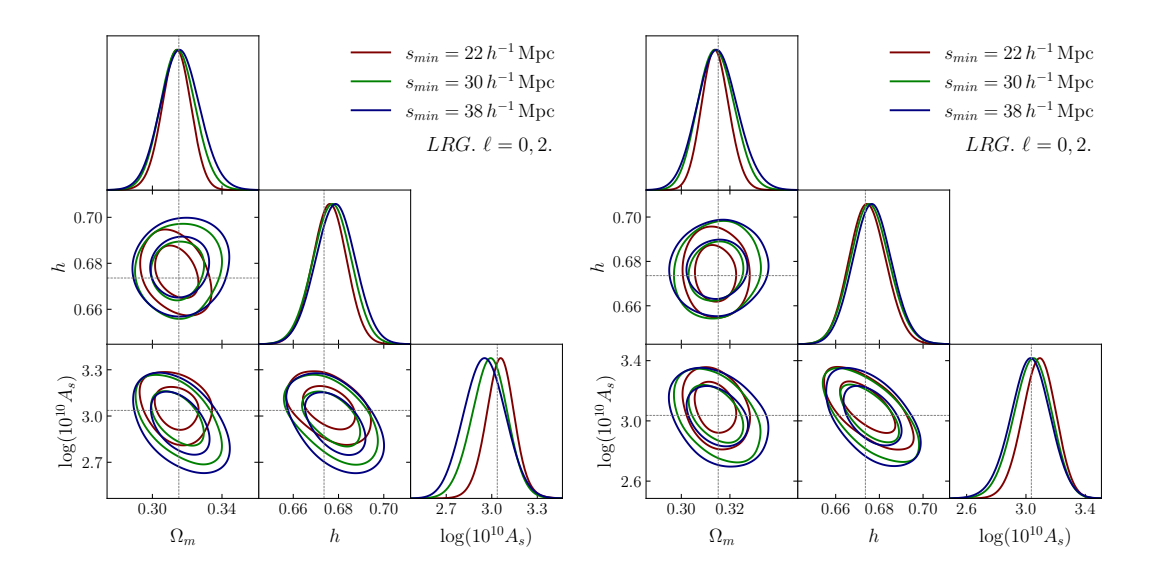


Figure 7. The triangular plot shows the posterior distribution obtained from the mean of 25 ABACUS-SUMMIT simulations using a non-rescaled covariance matrix for the LRG tracer following the *Full Modeling* methodology on the left side and the *ShapeFit* methodology on the right side. We plot three different ranges for the LRG tracers, a minimum scale $s_{min} = 22 \, h^{-1} {\rm Mpc}$ in red, $s_{min} = 30 \, h^{-1} {\rm Mpc}$ in green, and $s_{min} = 38 \, h^{-1} {\rm Mpc}$ in blue.

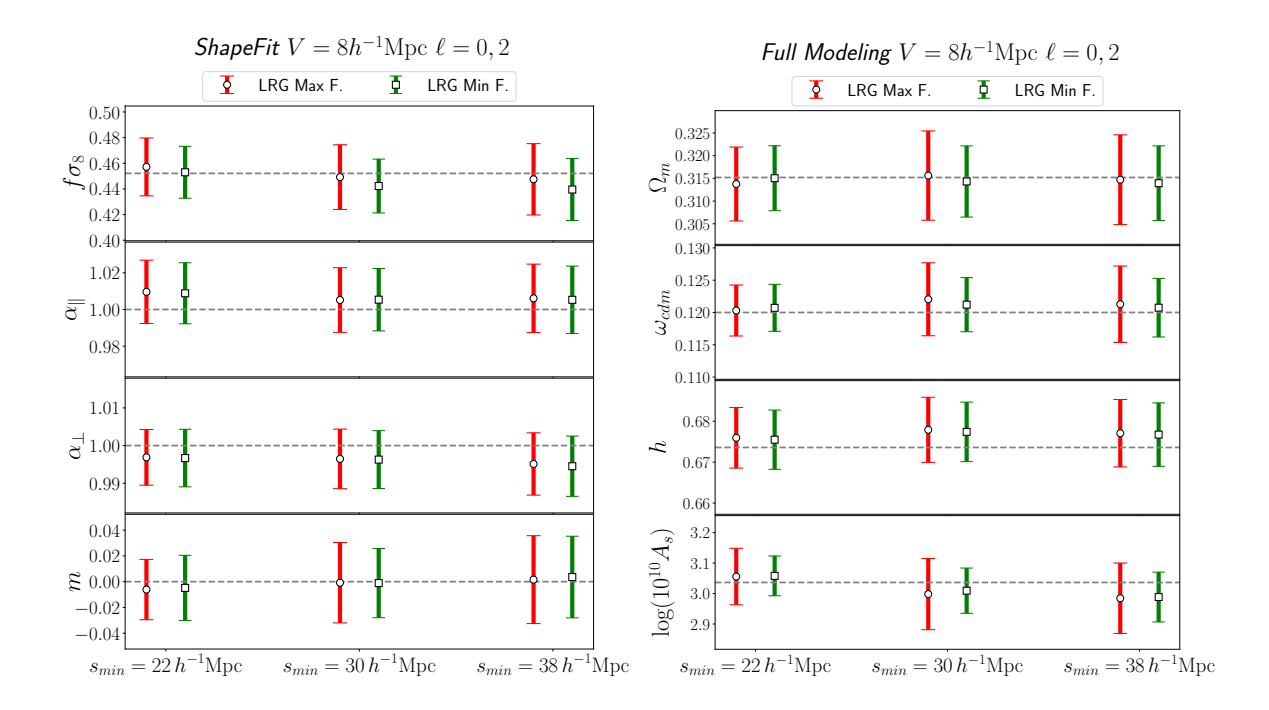


Figure 8. Error bar comparison for LRG using a volume of $8 h^{-3} \text{Gpc}^3$. The red bars were obtained using maximal freedom, while the red ones were obtained using minimal freedom. We show the model's behavior at various minimum scales, each one separated by 1 bin of $8 h^{-1} \text{Mpc}$. On the left side, we have the *ShapeFit* fits, while on the right side, we have the *Full Modeling* fits.

BASELINE

	Full Modeling (Max Freedom)						
\overline{V}	$s_{ m min}$	s_{\min} Ω_m		$\ln(10^{10}A_s)$			
V_1	$22 h^{-1}{ m Mpc}$	0.3138 ± 0.0081	0.6760 ± 0.0074	3.056 ± 0.093			
V_1	$30 h^{-1}{ m Mpc}$	0.3147 ± 0.0099	0.6771 ± 0.0083	2.98 ± 0.12			
V_1	$38 h^{-1}{ m Mpc}$	0.316 ± 0.011	0.6786 ± 0.0086	2.95 ± 0.13			
V_5	$22 h^{-1}\mathrm{Mpc}$	0.3146 ± 0.0037	0.6775 ± 0.0042	3.038 ± 0.044			
V_5	$30 h^{-1}{ m Mpc}$	0.3146 ± 0.0046	0.6768 ± 0.0052	3.003 ± 0.058			
V_5	$38 h^{-1}{ m Mpc}$	0.3144 ± 0.0050	0.6771 ± 0.0052	2.984 ± 0.067			
		ShapeFit (Ma	ax Freedom)				
V	s_{\min}	Ω_m	h	$\ln(10^{10}A_s)$			
V_1	$22 h^{-1}{ m Mpc}$	0.3140 ± 0.0055	0.6747 ± 0.0082	3.09 ± 0.11			
V_1	$30 h^{-1}{ m Mpc}$	0.3144 ± 0.0072	0.6758 ± 0.0088	3.04 ± 0.12			
V_1	$38 h^{-1}{ m Mpc}$	0.3149 ± 0.0081	0.6768 ± 0.0086	3.03 ± 0.13			
V_5	$22 h^{-1}{ m Mpc}$	0.3156 ± 0.0027	0.6772 ± 0.0043	3.044 ± 0.053			
V_5	$30 h^{-1}{ m Mpc}$	0.3153 ± 0.0036	0.6760 ± 0.0054	3.014 ± 0.061			
V_5	$38 h^{-1}{ m Mpc}$	0.3151 ± 0.0039	0.6771 ± 0.0055	2.999 ± 0.069			

Table 4. Constraints on our cosmological parameters when fitting our ABACUS LRG sample for three minimum scales when using different methodologies, *Full Modeling* methodology and *ShapeFit* methodology together with two different volumes $V_1 = 8 \, h^{-3} {\rm Mpc}^3$ and $V_5 = 40 \, h^{-3} {\rm Mpc}^3$.

Full Modeling (Min Freedom).

$s_{ m min}$	Ω_m	h	$\ln(10^{10}A_s)$
$22 h^{-1}\mathrm{Mpc}$	0.3150 ± 0.0072	0.6755 ± 0.0072	3.058 ± 0.065
$30 h^{-1}{ m Mpc}$	0.3139 ± 0.0082	0.6767 ± 0.0078	2.989 ± 0.082
$38 h^{-1} \mathrm{Mpc}$	0.314 ± 0.010	0.6786 ± 0.0080	2.96 ± 0.11

Table 5. Constraints to our parameters when fitting our ABACUS LRG sample for three minimum scales when using different methodologies, *Full Modeling* methodology.

$s_{ m min}$	$f\sigma_8$	$lpha_\parallel$	$lpha_{\perp}$	m
$22 h^{-1} \mathrm{Mpc}$	0.453 ± 0.020	1.009 ± 0.017	0.9967 ± 0.0076	$-0.004_{-0.018}^{+0.028}$
$30 h^{-1}{ m Mpc}$	0.442 ± 0.021	1.005 ± 0.017	0.9963 ± 0.0077	-0.001 ± 0.027
$38 h^{-1}{ m Mpc}$	0.440 ± 0.024	1.005 ± 0.018	0.9945 ± 0.0080	0.004 ± 0.032

Table 6. Constraints to our parameters when fitting our ABACUS LRG sample for three minimum scales when using different methodologies for *ShapeFit* methodology.

using the more restricted *Minimal* freedom configuration, this is true regardless of whether we employ the compressed or *Full Modeling* approach. However, throughout this work we opt for a conservative approach and designate the *Maximal* freedom scenario as our baseline configuration.

5.2 Extensions to Baseline Analysis

We will present three extensions to the main analysis we presented above. First we focus on the information we can extract from the hexadecapole of the correlation function, then we explore the possibility to constrain the spectral index n_s and finally we allow the Dark Energy equation of state evolve with the time using the (w_o, w_a) prescription.

5.2.1 Effect of including hexadecapole

In this subsection, we explore the effect of adding the hexadecapole in our baseline analysis. It is well known that the hexadecapole is considered to be the multipole where PT at first-loop starts to struggle to reproduce the small scales for both the 2-point correlation function and the power spectrum, particularly at small scales (below $30\,h^{-1}{\rm Mpc}$ in configuration space), where non-linear effects start to be important.

In Figure 9 we can observe the effect of including the hexadecapole in the compressed parameter space and the cosmological parameter space for three different ranges, $s_{min}=22$, 30, and $38\,h^{-1}{\rm Mpc}$. The fits following our baseline analysis are plotted in red, while fits adding hexadecapole are shown in green. Due to the difficulties in small scale model of the hexadecapole, we remove the bin $22\,h^{-1}{\rm Mpc}$ and maintain the bin $s_{min}=22\,h^{-1}{\rm Mpc}$ for the monopole and the quadrupole. This is done because when we include the smaller hexadecapole bin, we note that our posterior distribution becomes bimodal due to the appearance of a second region of the parameter space with high likelihood. However, this region has already been discarded by Planck to more than 3σ . Given that we don't trust our model at these smaller r scales, we opt to exclude this bin. The quantitative results are shown in Tables 3, 4, 7 and 8. In the compressed parameters, we note slight variations within the 1σ range for $f\sigma_8$, α_{\parallel} , α_{\perp} , and m. Similarly, the cosmological parameters exhibit consistent results, with Ω_m , h, and A_s all falling within the 1σ range.

On the other side, the error bars when we include the hexadecapole for the three minimum scales have a small reduction in *ShapeFit*. For $f\sigma_8$ the error bar is reduced by 0.26%-0.07% compared with the baseline analysis, for α_{\parallel} this change is 0.26%-0.30%, while α_{\perp} remains in 0.06%, and finally for m this change goes from an increase of 0.04% to

Full Modeling (M+Q+H)

$s_{ m min}$	Ω_m	h	$\ln(10^{10}A_s)$
$22 h^{-1} \mathrm{Mpc}$	$0.3138^{+0.0099}_{-0.0085}$	0.6707 ± 0.0072	$3.098^{+0.066}_{-0.082}$
$30 h^{-1}{ m Mpc}$	0.3094 ± 0.0082	0.6711 ± 0.0071	3.060 ± 0.095
$38 h^{-1}{ m Mpc}$	0.3107 ± 0.0093	0.6741 ± 0.0075	3.01 ± 0.13

Table 7. 1D constraints when fitting the ABACUS LRG mocks with (M+Q+H) and without (M+Q) the hexadecapole for three minimum scales for *Full Modeling*.

ShapeFit	(M+Q+H)

$s_{ m min}$	$f\sigma_8$	$lpha_\parallel$	$lpha_{\perp}$	m
$22h^{-1}{\rm Mpc}$	0.459 ± 0.017	$1.009^{+0.011}_{-0.012}$	$1.0015^{+0.0074}_{-0.0065}$	$-0.013^{+0.026}_{-0.023}$
$30h^{-1}{\rm Mpc}$	0.453 ± 0.022	$1.010^{+0.012}_{-0.013}$	0.9984 ± 0.0074	-0.017 ± 0.025
$38 h^{-1}{ m Mpc}$	0.451 ± 0.026	1.011 ± 0.014	0.9965 ± 0.0078	-0.007 ± 0.031
$30h^{-1}{ m Mpc}$	0.449 ± 0.025	1.005 ± 0.018	0.9965 ± 0.0079	-0.001 ± 0.031

Table 8. 1D constraints when fitting the ABACUS LRG mocks with (M+Q+H) and without (M+Q) the hexadecapole for three minimum scales for ShapeFit methodology.

a reduction of 0.08%. For *Full Modeling* we have a change in the error bars for Ω_m that goes from an increment of 0.13% to a decrease of 0.17%, for h we have a diminution in the error bars of 0.03% - 0.14%, while $\ln(10^{10}A_s)$ has a reduction in the error bars of 0% - 0.21%.

In conclusion, adding the hexadecapole does not significantly improve the results, even when removing specifically the lowest bin distance in order to prevent the problems on quasi-linear scale model. The main effect is slightly reducing the error on the *Full Modeling* analysis. However, we can notice that all the constraints remain below 1σ from the true value when we include the hexadecapole.

5.2.2 Exploring the impact of n_s free

The scalar spectral index, denoted as n_s , serves as a key parameter that characterizes the primordial power spectrum of density perturbations in the early universe. As mentioned in Section 4.6, in our standard approach, we fix this parameter to its Planck 2018 reported value of $n_s = 0.9649$ [75]. However, in this section, we incorporate this parameter into our methodology as one of the extensions of our baseline analysis. This extension enables a more comprehensive and complex exploration of the parameter space. In this section, we impose the following prior on n_s :

$$n_s: \mathcal{U}[0.5, 1.5]$$
 (5.1)

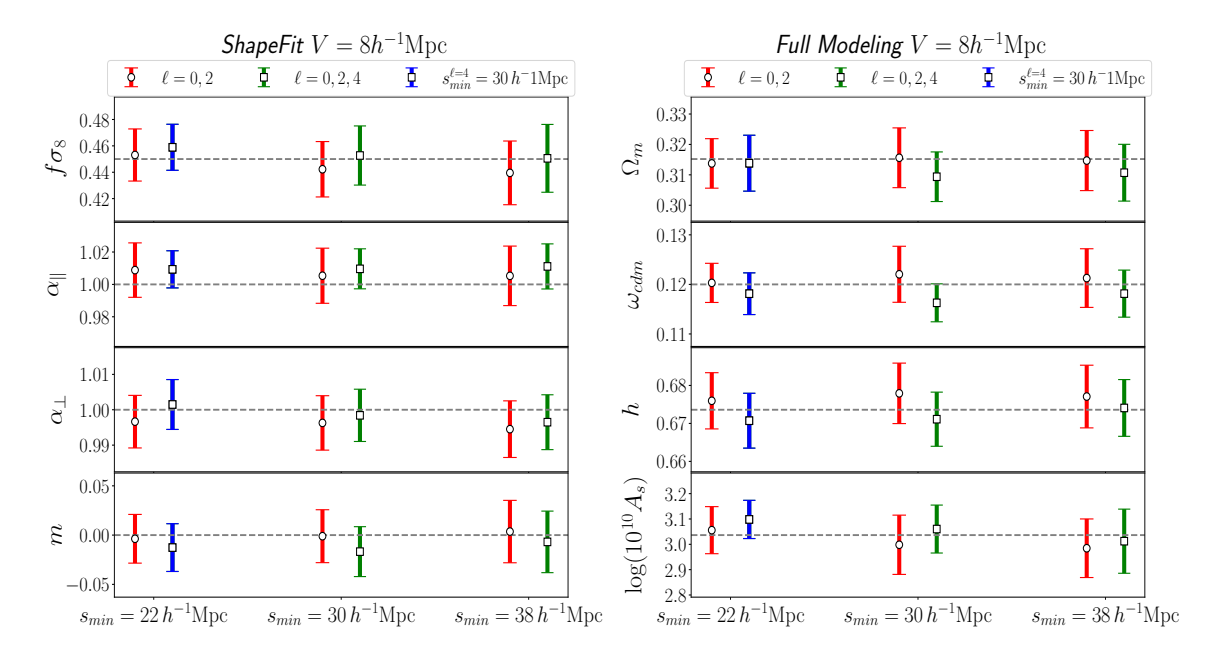


Figure 9. 1D constraints as a function of minimum scale for the LRGs using a volume of 8 h^{-1} Mpc. The results for the baseline analysis without the hexadecapole are shown in red while the results including the hexadecapole are shown in green. On the left side, we have the *ShapeFit* fits, while on the right side, we have the *Full Modeling* fits. The lower bin, represented in blue, has the same settings, but the bin $s_{min} = 22 h^{-1}$ Mpc is excluded for the hexadecapole.

Given the new degree of freedom included, the models become more complex, in order to maintain the precision of our emulator, we expand the number of multipoles utilized in the neural network to 90,000. Among these, 80,000 are allocated for training the network, while 5,000 served as a validation set. The remaining 5,000 are our test set dedicated to generating statistics for evaluating the model's performance.

Figure 10 shows the results of our analysis when varying minimum scales, $s_{\rm min}$, while treating n_s as a free parameter for the LRG sample and using Full Modeling. The results are presented for three distinct minimum scales, and each one has a different performance in the precision at a parameter is recovered. Our analysis consistently captures the expected values of all parameters within the 1σ uncertainty contour, including the extra parameter n_s . Specifically, for $s_{\rm min}=22\,h^{-1}{\rm Mpc}$, we achieve remarkable accuracy in determining h and $\log(10^{10}A_s)$ with 0.13σ and 0.13σ deviations from the true value respectively. Similarly, when $s_{\rm min}=30\,h^{-1}{\rm Mpc}$, our precision improves notably for Ω_m , h, and n_s with 0.13σ , 0.19σ and 0.05σ deviations respectively from the true value. Finally, when $s_{\rm min}=38\,h^{-1}{\rm Mpc}$, our analysis aligns exceptionally well with Ω_m and n_s within 0.07σ and 0.04σ deviations respectively. The resulting constraints on our parameters are summarized in Table 9 (to be compared with baseline analysis in Table 4).

This shows how the sensitivity with which we can recover parameters varies with the minimum (s_{\min}) scale when n_s is free. The distinct performance levels observed across different s_{\min} values underscore the importance of carefully selecting this parameter in cosmological analyses. We see that, $s_{\min} = 30 h^{-1}$ Mpc is the scale exhibiting the most robust performance across all parameters, except \mathcal{A}_s which is still predicted to within less than one sigma from

 n_s Free

$s_{ m min}$	Ω_m	h	$\ln(10^{10}A_s)$	n_s
$22 h^{-1} \mathrm{Mpc}$	0.307 ± 0.014	0.6746 ± 0.0076	$3.05^{+0.10}_{-0.12}$	0.975 ± 0.037
$30 h^{-1}{ m Mpc}$	$0.313^{+0.015}_{-0.017}$	0.6752 ± 0.0086	2.99 ± 0.15	0.967 ± 0.045
$38 h^{-1}{ m Mpc}$	0.314 ± 0.018	0.6773 ± 0.0089	2.96 ± 0.17	0.967 ± 0.050

Table 9. Summary of the constraints obtained when fitting the ABACUS LRG sample with our *Full Modeling* methodology for our three minimum scales and when we allow n_s to vary as a free parameter

the true value. Our results highlight the capability of our analysis to consistently capture parameters within one sigma uncertainty, highlighting its robustness in characterizing extended cosmological models.

The results presented in this section are built using our Full Modeling methodology only.

5.2.3 Exploring the impact of w_0 and w_a as free parameters

The parameters w_0 and w_a characterize the behavior of dark energy within the Chevallier-Polarski-Linder model [105, 106]. This model provides a framework to study an evolving equation of state for dark energy and is an extension of the cosmological constant Λ CDM model. The function $w(a) = w_0 + w_a(1-a)$ describes the evolution of the equation of state parameter over cosmic times, offering insights into the dynamic nature of dark energy throughout the universe's history.

In this subsection, we analyze two different extensions of our methodology. In the first, we incorporate variations of the parameter w_0 only into our baseline analysis. Then, in the second extension, we vary both w_0 and w_a and study their combined effect.

We expand our standard setup, to incorporate w_0 and w_a as additional parameters, and we use the resulting models to train a new neural network. To ensure the precision of our emulator, we increase the number of multipoles used to train and test our neural networks to 170,000 points. Of these, 150,000 are allocated for train the networks, with 10,000 designated for validation and the remaining 10,000 are our test set that evaluate the model's performance. We also apply the following priors to our parameters:

$$w_0: \mathcal{U}[-2,0]$$
 (5.2)

$$w_a: \mathcal{U}[-3,3] \tag{5.3}$$

Here, we only consider the extension of our *Full Modeling* methodology.

Let us first present our results for the extended methodology that only includes w_0 . Figure 11 shows the triangular plot of the constraints on the set of cosmological parameters, where we can see that our analysis yields parameter constraints that are all within 1σ from their true value. The $s_{\min} = 22 h^{-1} \text{Mpc}$ case shows better performance when recovering cosmological parameters with smaller 1σ contours, while also being more accurate when predicting A_s . The model presents a 0.34σ deviation for the true Ω_m value, 0.41σ for h, 0.05σ

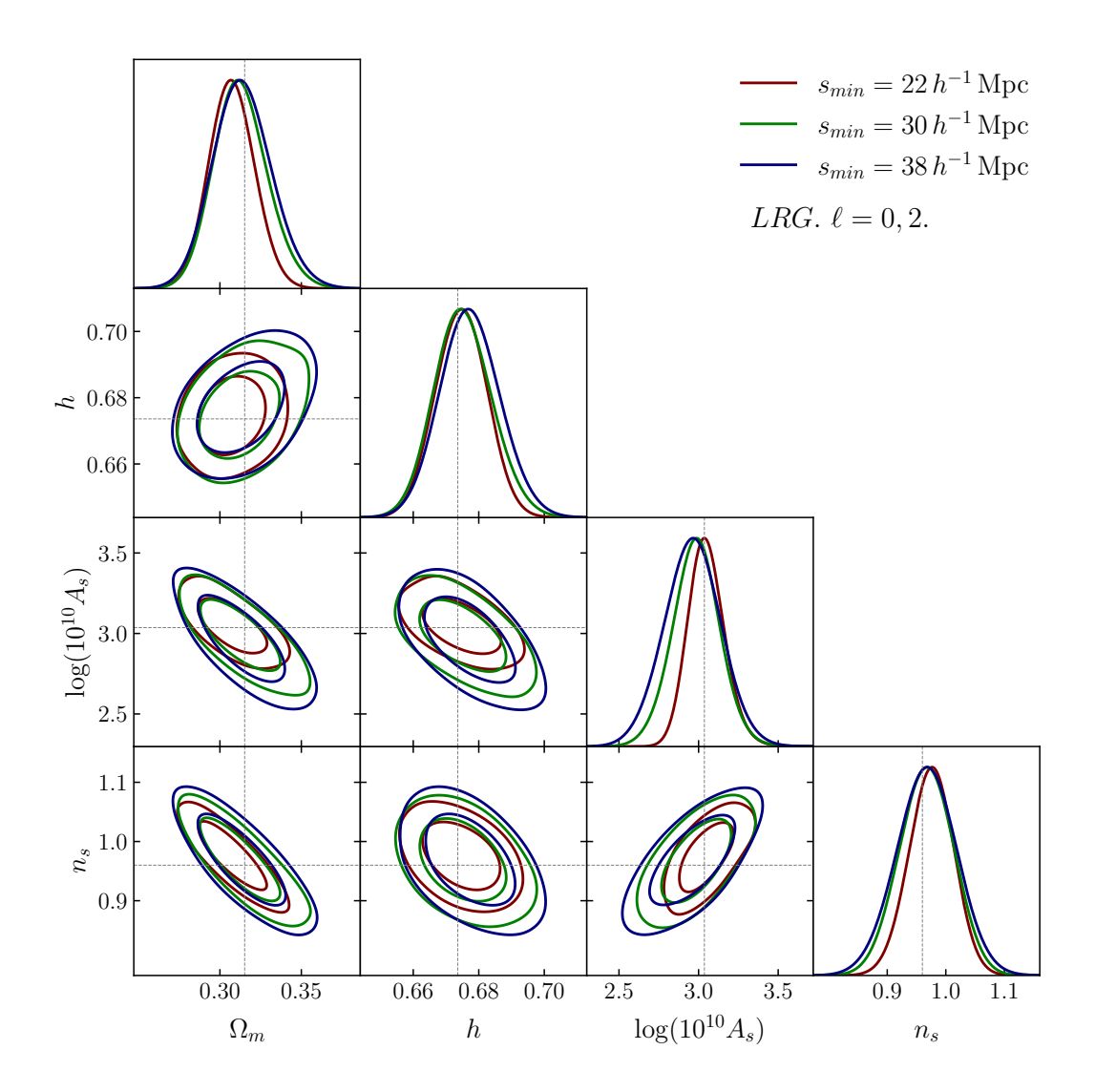


Figure 10. The triangular plot displays the posterior one-sigma and two-sigma contours of our baseline analysis when n_s is treated as a free parameter, using our *Full Modeling* methodology on the LRG sample. This plot illustrates the variation in predictions when adjusting the minimum scales. It is equivalent to the left panel of Figure 7 but with n_s set as a free parameter.

for $\log(10^{10}A_s)$, and $0.09\,\sigma$ for w_0 . Our extended model successfully recovers all parameters, including w_0 , showcasing its robustness when recovering the cosmological parameters.

Figure 12 shows the results for our second extension when we also add w_a as a free parameter and our extended model depends on both w_0 and w_a . As with the first extension, our analysis recovers all parameter constraints to within less than 1 σ from the true value for all parameters. The three models perform similarly well showing similar accuracy and prediction in most parameters, we note that the model with a minimum scale of $s_{\min} = 30 \, h^{-1} \mathrm{Mpc}$ and $s_{\min} = 38 \, h^{-1} \mathrm{Mpc}$ slightly perform better than $s_{\min} = 22 \, h^{-1} \mathrm{Mpc}$ when recovering A_s and Ω_m , but it still has the smaller error bars. The deviations for $s_{\min} = 22 \, h^{-1} \mathrm{Mpc}$ are within 1σ for this model and are $0.05 \, \sigma$ for Ω_m , $0.01 \, \sigma$ for h, $0.63 \, \sigma$ for $\log(10^{10} A_s)$, $0.47 \, \sigma$ for w_0 , and $0.69 \, \sigma$ for w_a .

Table 10 summarizes our final constraints for both extensions and all three scales. Our

 w_0 CDM Extension

$s_{ m min}$	Ω_m	h	$\ln(10^{10}A_s)$	w_0	w_a
$22 h^{-1} \mathrm{Mpc}$	$0.309^{+0.015}_{-0.021}$	$0.681^{+0.022}_{-0.019}$	3.031 ± 0.090	$-1.031^{+0.077}_{-0.10}$	0
$30 h^{-1}{ m Mpc}$	$0.313^{+0.017}_{-0.023}$	$0.679^{+0.025}_{-0.022}$	2.99 ± 0.12	$-1.011^{+0.085}_{-0.11}$	0
$38 h^{-1} \mathrm{Mpc}$	$0.314^{+0.018}_{-0.024}$	$0.681^{+0.026}_{-0.022}$	2.94 ± 0.13	$-1.014^{+0.090}_{-0.12}$	0
		w_0w_a CD	M Extension		
$22 h^{-1} \mathrm{Mpc}$	$0.314^{+0.020}_{-0.026}$	$0.674^{+0.027}_{-0.024}$	$3.13^{+0.11}_{-0.16}$	-0.88 ± 0.25	-0.67 ± 0.97
$30 h^{-1}{ m Mpc}$	$0.319^{+0.022}_{-0.027}$	0.673 ± 0.026	$3.07^{+0.14}_{-0.19}$	$-0.86^{+0.29}_{-0.26}$	-0.7 ± 1.0
$38 h^{-1} \mathrm{Mpc}$	$0.322^{+0.023}_{-0.029}$	0.673 ± 0.027	$3.07^{+0.16}_{-0.23}$	$-0.83^{+0.30}_{-0.27}$	-0.8 ± 1.1

Table 10. Constraints when fitting the ABACUS LRG mock for three minimum scales when we allow w_0 an w_a to vary as a free parameter and when using our *Full Modeling* methodology.

extended model successfully recovers all parameters, including w_0 and w_a , showing its ability to reliably recover the cosmological parameters.

5.3 All DESI tracers: LRG, ELG, QSO mocks

In this section, we expand our analysis to include fits to the ELG and QSO mocks introduced in Section 2. Additionally, we create a new dataset by fitting all three samples together, this is done by merging all three distinct data vectors. Each vector contributes to the total sum of the logarithm of the likelihood, which is subsequently fitted using our model.

As with our previous sections, we fit three iterations of our model, additionally, we perform all fits twice, once using our *ShapeFit* template and once using the *Full Modeling* approach.

Tables 11 and 12 show the constraints on all *ShapeFit* and *Full Modeling* parameters for all fits mentioned above. The tables demonstrate that, in general, all constraints are tighter for our smaller minimum scale of $s_{\min} = 22, h^{-1}{\rm Mpc}$. To visually compare these results more intuitively, Figure 13 summarizes them as a set of error bar plots that also include our previous LRG results from Section 5.1.1. It is worth noting that all results in the figure are within one standard deviation from their expected value, indicating good accuracy. Given that all results are consistent with their expected value and that our measurements at the smaller minimum scale are slightly more precise, we select this as our main result.

Figure 14 depicts the triangular plot of our complete shape model alongside our findings for $s_{\min} = 22, h^{-1}\text{Mpc}$. We observe that, generally, the constraints from LRG and ELG exhibit similar precision, with ELG being marginally more precise, while QSO constraints are comparatively less precise overall. This aligns with our expectations based on the different effective volumes of the samples, with ELG being the largest DESI sample and QSO being the smallest. Additionally, we observe that our combined fit matches the expected value of all parameters within less than one sigma, with a 0.23σ deviation for Ω_m , a 0.68σ deviation for h, and a 0.26σ deviation for $\log(10^{10}A_s)$.

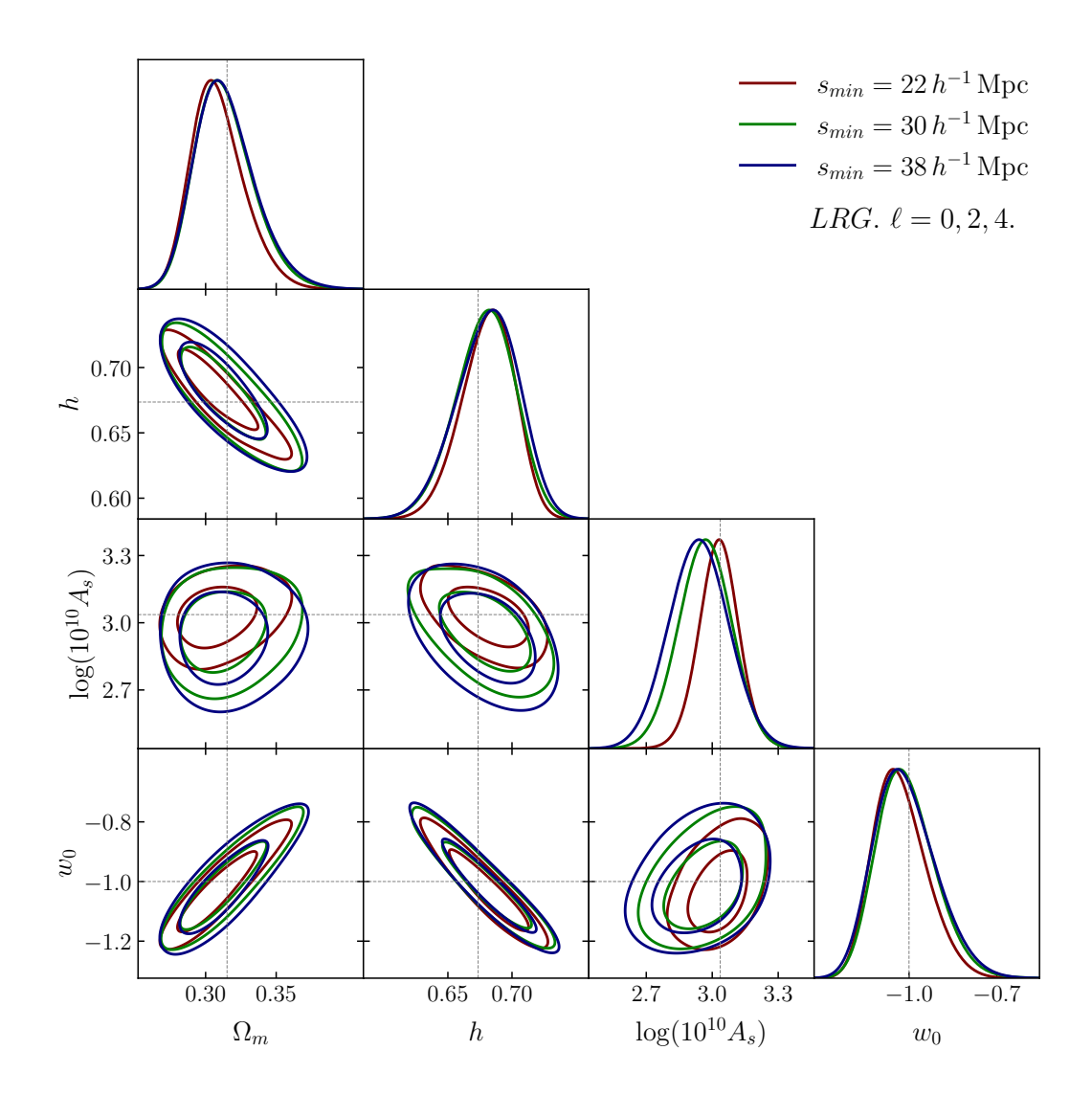


Figure 11. The triangular plot displays the posterior one-sigma and two-sigma contours of our baseline analysis when w_0 is treated as a free parameter, using our *Full Modeling* methodology on the LRG sample. This plot illustrates the variation in predictions when adjusting the minimum scales.

5.4 ShapeFit and Full Modeling methodology comparison

In this section, we transform ShapeFit from compressed parameters to cosmological parameters to be able to compare with $Full\ Modeling$ in the same parameter space. In Figure 15 we present a plot where we can observe small differences for ShapeFit and $Full\ Modeling$ when we fit the correlation function using LRG for a volume of $V=8\,h^{-3}{\rm Gpc}^3$ for the scales, $s_{min}=30\,h^{-1}{\rm Mpc}$. In particular, we observe a good agreement for the Maximal Freedom, Minimal Freedom, the case when we include the hexadecapole and the n_s extension having a similar constraining power.

First, we look at the baseline analysis, which shows good performance as we can notice from Table 4, where for Ω_m , we have nearly the same results in both methodologies, with a central value difference in the range of 10^{-3} and error bars of $0.68\sigma_{FM} < \sigma_{SF} < 0.74\sigma_{FM}$ being ShapeFit more constrictive for the three minimum scales. For h, we have a similar result

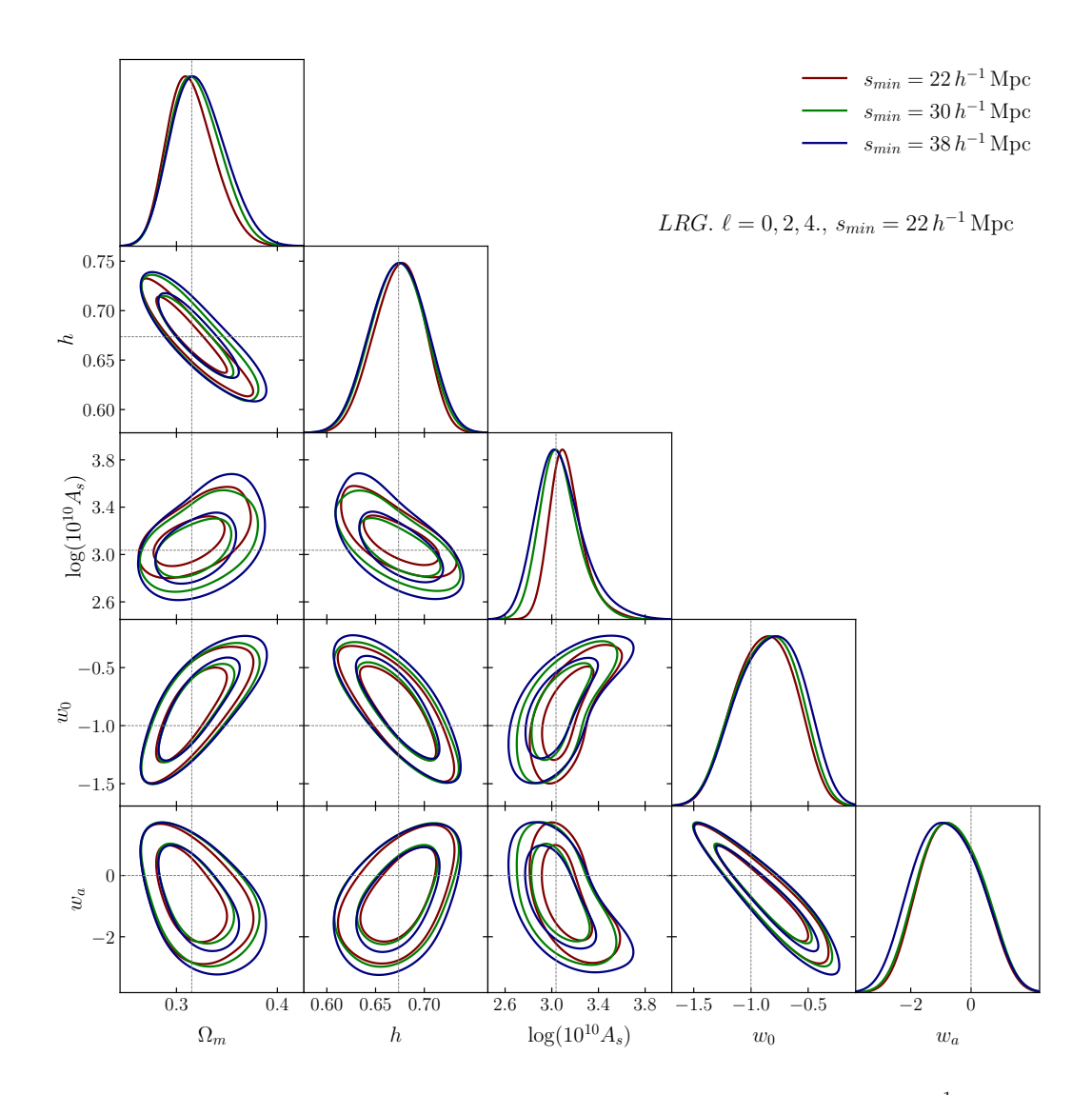


Figure 12. This plot shows the error bar comparison for LRG using a volume of 8 h^{-1} Mpc. The red bars were obtained using maximal freedom, while the red ones were obtained using minimal freedom. We show the model's behavior at various minimum scales, each one separated by 1 bin of 8 h^{-1} Mpc. On the left side, we have the *ShapeFit* fits, while on the right side, we have the *Full Modeling* fits.

obtaining a difference in the central value of around 10^{-3} and error bars of $1.11\sigma_{FM} < \sigma_{SF} < 1.0\sigma_{FM}$ this time, shape fit shows less constrictive power. In the last parameter, $\ln(10^{10}A_s)$, the central value shows a difference of the order of 10^{-3} with error bars $1.0\sigma_{FM} < \sigma_{SF} < 1.18\sigma_{FM}$, ShapeFit again is less constrictive.

The Minimal Freedom case shows similar performance, the statistic is detailed in Table 13, where we obtain for Ω_m roughly the same results in the central value with a difference of the order of 10^{-3} and error bars $0.76\sigma_{FM} < \sigma_{SF} < 0.80\sigma_{FM}$ being ShapeFit more constrictive. For h, we have a central value which shows a difference around 10^{-3} and error bars of $1.05\sigma_{FM} < \sigma_{SF} < 1.1\sigma_{FM}$, with ShapeFit with less constrictive power. Finally, $\ln(10^{10}A_s)$ shows a central value difference of the order of 10^{-2} with error bars $1.09\sigma_{FM} < \sigma_{SF} < 1.33\sigma_{FM}$, again ShapeFit less constrictive.

When we include the hexadecapole in the baseline analysis, we obtain similar constrain-

DESI tracers

$s_{ m min}$	Ω_m	h	$\ln(10^{10}A_s)$
ELG Full Modeling			
$22 h^{-1}\mathrm{Mpc}$	0.314 ± 0.011	0.6779 ± 0.0066	$3.015^{+0.085}_{-0.10}$
$30 h^{-1}{ m Mpc}$	0.314 ± 0.011	0.6761 ± 0.0072	3.014 ± 0.092
$38 h^{-1}{ m Mpc}$	$0.316^{+0.012}_{-0.014}$	0.6769 ± 0.0076	$3.00^{+0.11}_{-0.10}$
QSO Full Modeling			
$\frac{1}{22 h^{-1} \mathrm{Mpc}}$	0.309 ± 0.017	0.681 ± 0.014	3.02 ± 0.14
$30 h^{-1}{ m Mpc}$	0.310 ± 0.019	0.683 ± 0.015	3.01 ± 0.16
$38 h^{-1}{ m Mpc}$	0.3139 ± 0.0073	0.6776 ± 0.0057	2.983 ± 0.076
COMBINED Full Modeling			
$\frac{1}{22 h^{-1} \mathrm{Mpc}}$	0.3139 ± 0.0057	0.6770 ± 0.0050	3.021 ± 0.060
$30 h^{-1}{ m Mpc}$	0.3129 ± 0.0059	0.6772 ± 0.0057	3.002 ± 0.062
$38 h^{-1} \mathrm{Mpc}$	$0.309^{+0.015}_{-0.021}$	$0.681^{+0.022}_{-0.019}$	3.031 ± 0.090

Table 11. Constraints to our *Full shape* (top) and *ShapeFit* (bottom) parameters when fitting our ABACUS ELG, QSO and Combined samples for all three minimum scales explored.

ing power in both analyses. In Table 13, we can see that for Ω_m , we have a central value with a difference around 10^{-3} and error bars of $0.71\sigma_{FM} < \sigma_{SF} < 0.77\sigma_{FM}$ being ShapeFit more constrictive for all the minimum scales. For the h parameter, we have a central value with a difference around 10^{-3} and error bars of $1.00\sigma_{FM} < \sigma_{SF} < 1.11\sigma_{FM}$, with ShapeFit less constrictive. Lastly, $\ln(10^{10}A_s)$, shows a central value difference of the order of 10^{-2} with error bars $1.0\sigma_{FM} < \sigma_{SF} < 1.09\sigma_{FM}$, ShapeFit being less constrictive.

On the other hand, when we include n_s as a model extension, we implement the extra parameter n, in the ShapeFit methodology, so we vary α_{\perp} , α_{\parallel} , $f\sigma_8$, m and n, then, we convert these parameters into cosmological parameter using $n=n_s-n_{\rm ref}$ [94], these results are in Table 13. We notice that for Ω_m , we have a central value of the order of 10^{-3} , with a difference around $0.72\sigma_{FM} < \sigma_{SF} < 0.93\sigma_{FM}$ being ShapeFit more constrictive. In the case of h, we have a central value difference of the order 10^{-3} and error bars which show a difference of $0.99\sigma_{FM} < \sigma_{SF} < 1.11\sigma_{FM}$. Then, we have the $\ln(10^{10}A_s)$ parameter, which shows a central value difference of the order of $< 10^{-2}$ with error bars $0.88\sigma_{FM} < \sigma_{SF} < 1.18\sigma_{FM}$. Finally, the n_s parameter shows a difference in the central value of the order of 10^{-3} while the error bars are $1.32\sigma_{FM} < \sigma_{SF} < 1.54\sigma_{FM}$ with ShapeFit being less constrictive.

So far, we extensively explore two distinct methodologies for predicting the recovery of cosmological parameters: *ShapeFit* and *FullModeling*. We demonstrate the accuracy and efficacy of both approaches for the baseline analysis.

s_{\min}	$f\sigma_8$	$lpha_\parallel$	$lpha_{\perp}$	m		
ELG ShapeFit						
$22 h^{-1} \mathrm{Mpc}$	0.411 ± 0.019	1.007 ± 0.014	0.9971 ± 0.0076	$-0.001^{+0.023}_{-0.020}$		
$30 h^{-1}{ m Mpc}$	$0.415^{+0.014}_{-0.016}$	1.007 ± 0.014	0.9960 ± 0.0070	-0.004 ± 0.027		
$38 h^{-1}{ m Mpc}$	$0.415^{+0.016}_{-0.018}$	1.007 ± 0.015	$0.9959^{+0.0066}_{-0.0075}$	-0.003 ± 0.030		
QSO ShapeFit						
$22 h^{-1}{\rm Mpc}$	0.385 ± 0.023	1.006 ± 0.026	0.995 ± 0.015	-0.011 ± 0.027		
$30 h^{-1}{ m Mpc}$	0.385 ± 0.025	1.004 ± 0.027	0.994 ± 0.015	-0.006 ± 0.035		
$38 h^{-1} \mathrm{Mpc}$	$0.384^{+0.025}_{-0.029}$	1.004 ± 0.027	0.994 ± 0.015	0.003 ± 0.038		

Table 12. Constraints to our *Full shape* (top) and *ShapeFit* (bottom) parameters when fitting our ABACUS ELG, QSO, and Combined samples for all three minimum scales explored.

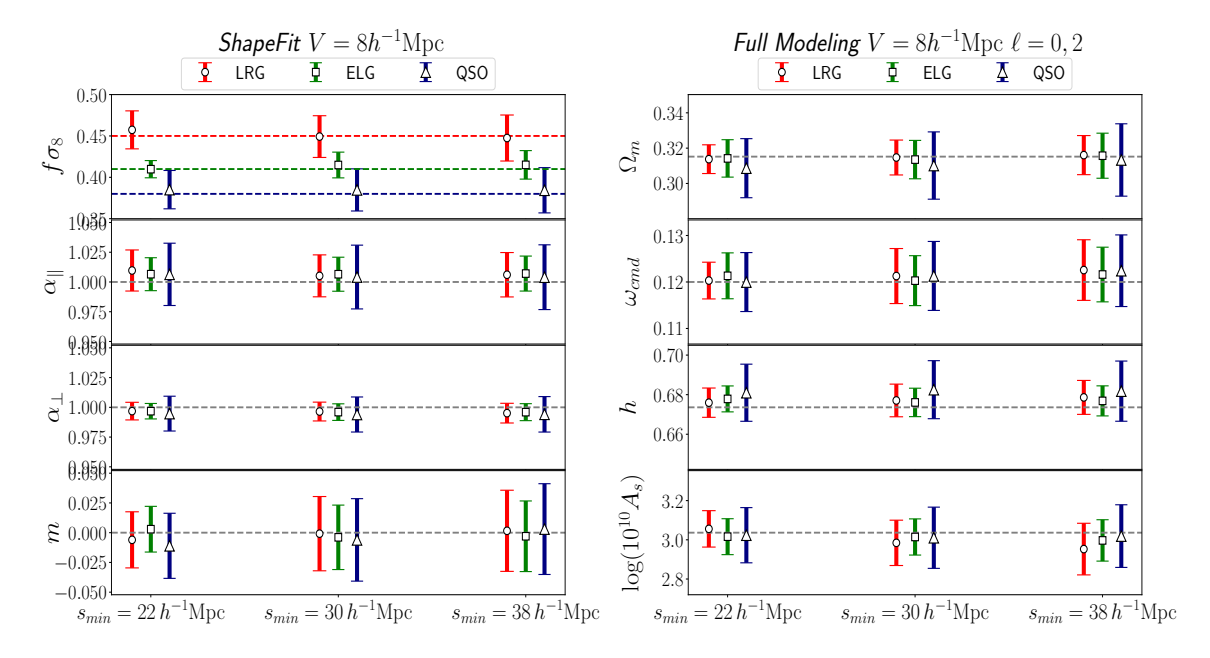


Figure 13. Error bar plots on LRG (red), ELG (green), and QSO (blue) constraints for three minimum scales and for *Shape Fit* (left) and *Full Modeling* (right) parameters. The black dashed lines show the true value of the parameters (note that the true value of $f\sigma_8$ is dependent on redshift).

6 Comparisons with others Effective Field Theory models

As stated at the beginning of this manuscript, our EFT-GSM model is one of four EFT theories utilized in the analysis of galaxy Full-Shape within DESI year one data. In the companion paper [52], the three models in Fourier space (FS) (namely, the Velocileptors model of

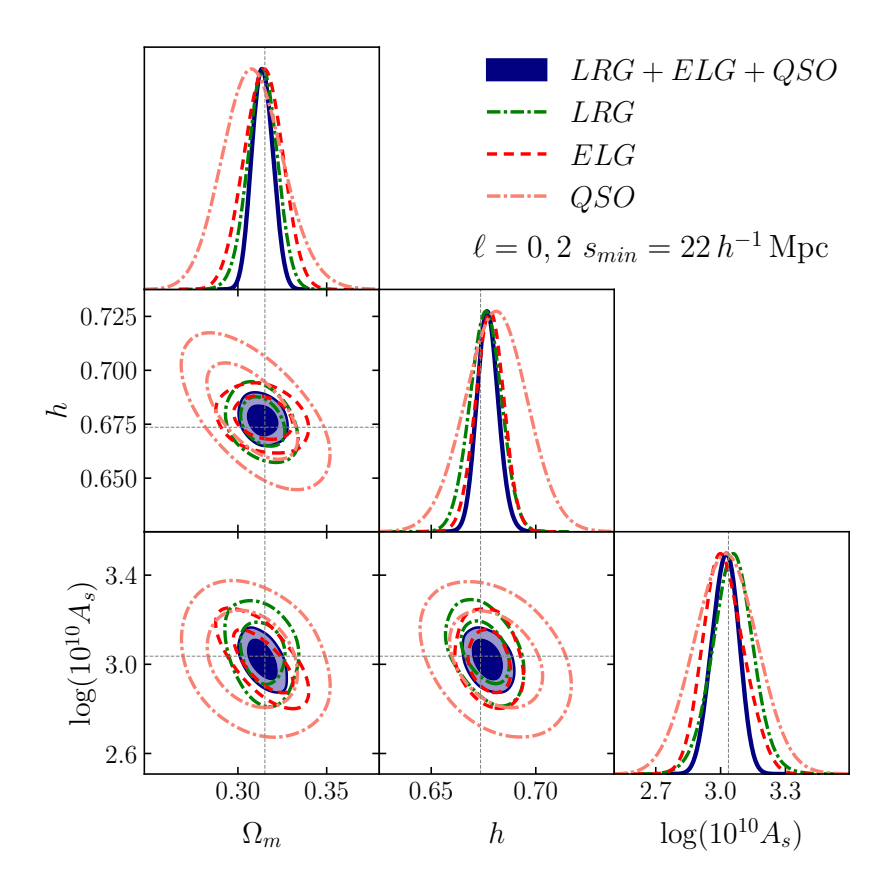


Figure 14. We present results for our three tracers: LRG (green dashed lines), ELG (red dashed lines) and QSO (salmon dashed lines). We also include the resulting contour of the combined LRG + ELG + QSO (blue solid lines and contours), and the expected value of each parameter (gray faded lines).

[51], the Folps ν model of [48], and the PyBird model of [46]) are compared to each other, this section extends the comparison by showing how their results align with our configuration space (CS) counterpart presented in this work. We highlight that our GSM-EFT methodology is the only model fully developed in CS out of the four models considered here.

We divide this comparison into two parts. The first section 6.1 shows two results where the analysis of the three models we are comparing with is done in FS. The first result is a direct comparison between our parameter constraints in CS and the original FS results of Velocileptors, Folps ν , and PyBird. The second comparison involves using a different implementation of these three codes, where we calculate their results using the desilike 11 tool. This tool is a compendium of all the methodologies required for the likelihood analysis of DESI. It's designed to provide a common framework for all analyses. Therefore, it allows us to execute all the important parts of our methodologies using the same tool for all models. This includes the MCMC sampler, likelihood estimations, methods for fabricating the input linear power spectrum and so on. Therefore when using desilike, the only difference between the methodologies used to analyze each of the four models is the method used to compute the redshift space multipoles from the input linear power spectrum.

Working with desilike is not only useful because it allows us to standardize the method-

¹¹https://github.com/cosmodesi/desilike/

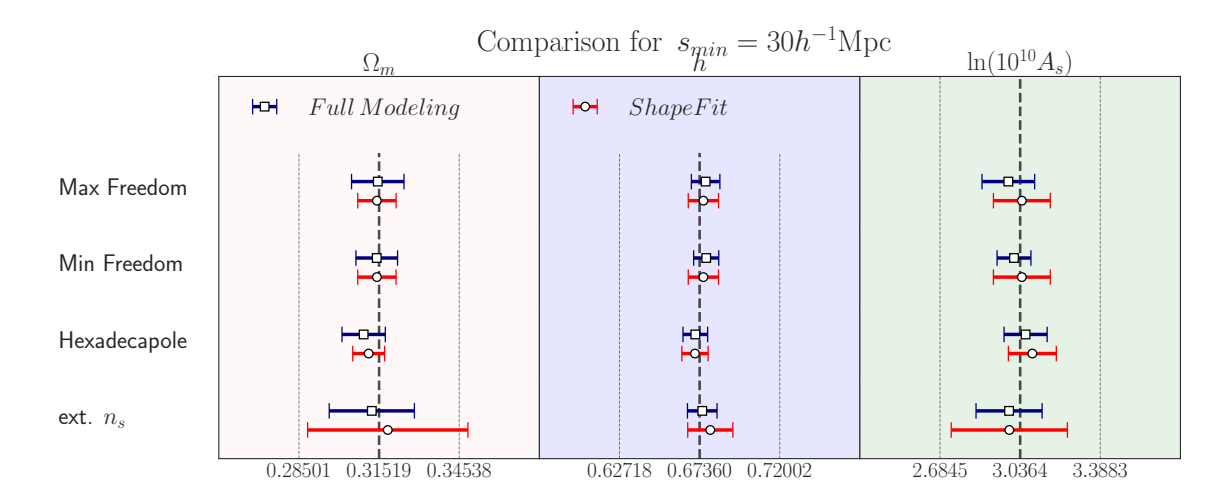


Figure 15. Comparison of the *Full Modeling* and *ShapeFit* methodologies in the cosmological parameter space, the red bars and the blue bars represent respectively the *ShapeFit* and the *Full Modeling* results obtained using the mean of the 25 realizations of the ABACUS-SUMMIT simulations with a non-rescaled covariance matrix when we fitted the monopole and quadrupole.

Cosmological Parameter Constraints						
Min Freedom						
\overline{T}	s	Ω_m	h	$\ln(10^{10}A_s)$		
$\overline{\mathrm{FM}}$	22	0.3150 ± 0.0072	0.6755 ± 0.0072	3.058 ± 0.065	-	-
FM	30	0.3139 ± 0.0082	0.6767 ± 0.0078	2.989 ± 0.082	-	-
FM	38	0.314 ± 0.010	0.6786 ± 0.0080	2.96 ± 0.11	-	-
SF	22	0.3144 ± 0.0058	0.6743 ± 0.0080	3.082 ± 0.087	-	-
SF	30	0.3146 ± 0.0062	0.6758 ± 0.0082	3.01 ± 0.10	-	-
SF	38	0.3155 ± 0.0077	0.6783 ± 0.0085	22.97 ± 0.12	-	-
			Hexadecapol	e		
$\overline{\mathrm{FM}}$	22	$0.3138^{+0.0099}_{-0.0085}$	0.6707 ± 0.0072	$3.098^{+0.066}_{-0.082}$	-	
FM	30	0.3094 ± 0.0082	0.6711 ± 0.0071	3.060 ± 0.095	-	-
FM	38	0.3107 ± 0.0093	0.6741 ± 0.0075	3.01 ± 0.13	-	-
SF	22	0.3142 ± 0.0065	0.6684 ± 0.0072	3.117 ± 0.081	-	-
SF	30	0.3113 ± 0.0060	0.6709 ± 0.0076	3.09 ± 0.11	-	-
SF	38	0.3128 ± 0.0072	0.6730 ± 0.0083	3.07 ± 0.13	-	-
			n_s			
\overline{T}	s	Ω_m	h	$\ln(10^{10}A_s)$	n_s	
FM	22	0.307 ± 0.014	0.6746 ± 0.0076	$3.05^{+0.10}_{-0.12}$	0.975 ± 0.037	-
FM	30	$0.313^{+0.015}_{-0.017}$	0.6752 ± 0.0086	2.99 ± 0.15	0.967 ± 0.045	-
FM	38	0.314 ± 0.018	0.6773 ± 0.0089	2.96 ± 0.17	0.967 ± 0.050	-
SF	22	$0.326^{+0.033}_{-0.038}$	0.681 ± 0.013	$2.97^{+0.25}_{-0.29}$	0.93 ± 0.14	-
SF	30	$0.319_{-0.037}^{+0.031}$	$0.680^{+0.013}_{-0.015}$	2.99 ± 0.27	0.96 ± 0.14	-
SF	38	$0.317^{+0.031}_{-0.038}$	$0.680_{-0.015}^{+0.013}$	3.01 ± 0.30	0.97 ± 0.15	-

Table 13. Constraints on our parameters when fitting our ABACUS LRG sample for three minimum scales when using $Full\ Modeling\ methodology$ and $ShapeFit\ methodologies$.

Model	Description
Folps- ν	EPT/EFT with beyond-EdS kernels [48]
PyBird	EPT /EFT [46]
Velocileptors	LPT/EFT with the possibility to run EPT/EFT [51].

Table 14. Brief description of the models compared in FS

ology between codes, but it also provides a standardized tool to transform FS multipoles into the CS. Therefore, it permits us to reanalyze the Velocileptors, Folps ν , and PyBird results, this time in CS. Section (6.2) shows how our EFT-GSM results compare with these new CS model constraints.

Throughout this whole section, we present all analyses in both *Full Modeling* and *Shape-Fit* configurations. Table 14 provides a short description of the codes used in this comparison. For a full description of the codes and individual performance, we refer the reader to the companion papers.

The four models utilize distinct conventions for their different galaxy-halo bias parameters. The translation between these conventions can sometimes be challenging to reproduce across all models. Therefore, in this study and its companion paper, we concentrate only on cases where this mapping is well-defined. While [51] explores the two cases minimal and maximal freedom, all comparisons presented here are done using only the minimal freedom configuration. This is done because our maximal freedom GSM-EFT model does not implement the tidal bias parameter of [52], and therefore our maximal freedom definition is not equivalent to one of the other models.

The definitions of minimal freedom for FS models are presented in [52], equations 4.15 and 4.16. Our comparisons are conducted by fitting the mean of the Abacus mocks using our covariance matrix without any re-scaling, which corresponds to having a volume of $V=8h^{-1}{\rm Mpc}$.

6.1 Comparison with EFT models in Fourier Space

As stated above, throughout this section, we present a set of results from analyses conducted in FS. All of these FS analyses select the same fiducial settings as those utilized in the companion paper. Therefore, we fit both the monopole and quadrupole up to $k_{\text{max}} = 0.25h^{-1}\text{Mpc}$. We begin this section by introducing a comparison between our CS results and the original FS results of Velocileptors, Folps ν , and PyBird. These comparisons are done for all three tracers: LRG, ELG, and QSO. We utilize the priors presented in Tables 1, 2, and 3 of the companion paper [52].

Figure 16 shows a set of triangular plots with the constraints we get using our Full Modeling (left panels) and ShapeFit (right panels) configurations, for our LRG (top panels), ELG (intermediate panels), and QSO (bottom panels) data respectively. It is important to notice that the posteriors of the FS results are generated with the original codes and are the same as those analyzed in the companion paper. We observe that the 1- σ contours of our GSM-EFT model align with those from the FS models showing very good agreement, while our model gives slightly narrower constraints. The observed difference between results may not be unexpected, considering that not all analyses are conducted in the same space and are not done with one standardized framework.

We observe that our CS constraints consistently yield smaller values compared to the three FS results obtained from other codes. Additionally, this trend holds true for all three tracers. As we mentioned, we have not standardized our framework in terms of MCMC sampler, likelihood evaluation and the fitting ranges between FS and CS are not exactly equivalent, which could explain the differences observed between methodologies. With this in mind, we test how our model compares with the rest when all the FS models are analyzed using the common framework from desilike. Figure 17 shows the results from this analysis and compares it with our GSM-EFT results. This comparison is complementary to the analysis of the next sub-section, where we use the desilike framework to redo all likelihood analysis in CS instead. These tests are intended as a verification that the differences observed so far are still present when we homogenize our analysis with desilike. Tables 15 and 16 present the quantitative results of this FS desilike analysis. Before analysing desilike results we verified that the results that the Full Modeling and ShapeFit constraints and errors were consistent between the original pipeline and their implementation within desilike. As we highlight in the next section, the difference found between FS and CS is also found in the CS implementation of the FS models, and is larger than the difference found between FS results with different pipelines.

6.2 Comparison with EFT models in Configuration space with DesiLike

In this final section we discuss the performance of all four models in CS. It is important to note that the Velocileptors, $Folps\nu$, and PyBird, models work in FS by construction. The CS counterparts of the original FS code are also implemented in desilike, the transformation between one space and the other is done using the Hankel transform of the FS multipoles,

$$\xi_{\ell}(s) = \frac{(-i)^{\ell}}{2\pi^2} \int dk k^2 P_{\ell}(k) j_{\ell}(ks)$$
 (6.1)

The Hankel transform is implemented in the $cosmoprimo^{12}$ package using the fftlog algorithm. For the Hankel transform we used a $k_{min} = 10^{-4}$ and $k_{max} = 0.6$. Beyond 0.6, there is a Gaussian damping.

Figure 18 shows the comparison between our GSM-EFT results and the desilike configurations space versions of Velocileptors, Folps ν , and PyBird. The left panel shows the Full Modeling results and the right panel the ShapeFit counterparts for the LRG sample and for different values of s_{min} . We observe good agreement between the models at all scales, we also note that there is slightly more dispersion than the one we observed in the FS analysis, which may be related to the sensitivity of the model to the parameters used in the Hankel transform. In order to getting a closer look, Figure 19 shows the triangular plot for both methodologies for $s_{min} = 30$. We observe that the contours are all well aligned with each other, and most of them are centered within less than 1σ from the true values. Tables 15 and 16 present the quantitative results of the CS with desilike. We notice that the errors obtained from the FS models in CS are consistently lower than their counterparts in FS, confirming the conclusion of the past section that CS provides slightly smaller error bars. The error bars of GSM-EFT are smaller than the mean error by 5-10 percent depending on the parameter. We consider the level of agreement to be reasonable given that the only model fully developed in CS is GSM-EFT and the others are generated from transforming the multipoles which may add a layer of potential numeric errors that require to be explored by tuning the internal parameters of

¹²https://github.com/cosmodesi/cosmoprimo/

Model	Space	Ω_m	h	$\ln(10^{10}A_s)$
Velocileptors LPT	FS	0.309 ± 0.012	0.6739 ± 0.0089	$3.030^{+0.083}_{-0.097}$
${\tt Folps}\nu$	FS	0.309 ± 0.011	0.6740 ± 0.0091	$3.051^{+0.083}_{-0.097}$
Pybird	FS	$0.311^{+0.012}_{-0.010}$	0.6737 ± 0.0090	3.03 ± 0.11
Velocileptors LPT	CS	0.3117 ± 0.0086	0.6757 ± 0.0076	3.008 ± 0.089
${\tt Folps}\nu$	CS	0.3138 ± 0.0093	0.6782 ± 0.0077	2.989 ± 0.093
Pybird	CS	0.3095 ± 0.0087	0.6762 ± 0.0086	$3.01^{+0.10}_{-0.12}$
GSM-EFT	CS	0.3139 ± 0.0082	0.6767 ± 0.0078	2.989 ± 0.082
GSM-EFT-22	CS	0.3150 ± 0.0072	0.6755 ± 0.0072	3.058 ± 0.065

Table 15. Constraints on *Full modeling* parameters when fitting the ABACUS-LRG for different models and different spaces, minimal freedom, using desilike compared with this work.

the Hankel transform some of the parameters, such as the binning and the value of k_{max} . A careful exploration of the dependence of the configuration space constraints on the numerical precision on the Hankel transform and the exploration of the differences between precision depending of the different spaces is left of a future job.

7 Conclusions

In preparation for the analysis of the upcoming first batch of DESI data, it is imperative to analyze and test the tools that will be used to extract cosmological information. This includes testing different configurations and degrees of freedom that models can have when predicting the full-shape of galaxy two-point statistics. In particular, there is a lot of interest in understanding the differences in accuracy and precision between compressed methodologies like the *Standard* and *Shape-Fit* methods, which are more model agnostic, and direct methods like the *Full Modeling* methodology where a particular cosmological model is selected a priori.

Currently, four independent methodologies that model the redshift space clustering statistics are being developed and tested within the collaboration in preparation for the first data release. These are the PyBird, FOLPS ν , and Velocileptors methodologies, all of which study the FS power spectrum of tracers. The fourth method is our own EFT-GSM methodology, which is the only approach working on CS.

Throughout this work, we have analyzed the performance of our GSM-EFT model, along with some extensions that allow us to explore a wider parameter range, in recovering the cosmological information from a new suite of 25 ABACUS-SUMMIT mocks. These mocks have been independently populated with different tracers of matter to generate samples resembling ELGs, LRGs, QSOs. Here, we have analyzed all three samples independently, and we also examine a combined sample. We have compared our constraints with those produced by the

Model	Space	$f\sigma_8$	$lpha_\parallel$	$lpha_{\perp}$	m
Velocileptors LPT	FS	0.448 ± 0.024	1.004 ± 0.021	0.9987 ± 0.0099	$-0.023^{+0.039}_{-0.032}$
Folps $ u$	FS	0.453 ± 0.024	1.004 ± 0.021	0.9989 ± 0.0099	$-0.024^{+0.037}_{-0.031}$
Pybird	FS	0.451 ± 0.026	1.001 ± 0.021	0.9995 ± 0.010	$-0.024^{+0.043}_{-0.031}$
Velocileptors LPT	CS	0.444 ± 0.022	1.002 ± 0.017	0.9972 ± 0.0078	$-0.009^{+0.031}_{-0.028}$
Folps $ u$	CS	0.447 ± 0.023	1.002 ± 0.017	0.9982 ± 0.0076	$-0.012^{+0.034}_{-0.031}$
Pybird	CS	0.451 ± 0.024	$1.012^{+0.020}_{-0.018}$	0.9957 ± 0.0074	-0.046 ± 0.032
GSM-EFT-30	CS	0.442 ± 0.021	1.005 ± 0.017	0.9963 ± 0.0077	-0.001 ± 0.027
GSM-EFT-22	CS	0.453 ± 0.020	1.009 ± 0.017	0.9966 ± 0.0074	$-0.004^{+0.027}_{-0.021}$

Table 16. Constraints on *ShapeFit* parameters when fitting the ABACUS-LRG for different models and different spaces, minimal freedom using desilike compared with this work.

three other FS models when transforming their predictions into CS. The analysis presented here utilizes our optimized C-code tool introduced in this paper, which computes the CS multipoles of our GSM-EFT model. Furthermore, we have optimized our methodology by employing Neural Networks to construct surrogate models of our GSM-EFT models, accelerating their evaluation and thus reducing the convergence time required to obtain cosmological constraints.

We have analyzed the ability of our Full Modeling configuration to recover the ABACUS –SUMMIT LRG cosmology under variations in the volume of the simulation. This was achieved by running our analysis on volumes of $8, h^{-3}, \operatorname{Gpc}^3, 40, h^{-3}, \operatorname{Gpc}^3, \operatorname{and} 200, h^{-3}, \operatorname{Gpc}^3, \operatorname{respectively}$, which correspond to approximately the first and fifth years of DESI observations, and a much larger volume than DESI, respectively. We find that our methodology is relatively robust to variations in volume, with all parameters being recovered to within 1σ of their original values, with the exception of the values of h and $\ln(10^{10}A_s)$ for the larger volume, which are recovered to within 1.14σ and 1.4σ , respectively. Throughout this work, we choose to report our results based on an $8, h^{-3}, \operatorname{Gpc}^3$ box, as this approximates the size of the DESI year one volume.

We have also tested how our results vary in our baseline analysis of the LRG sample under variations of the minimum scale utilized in our analysis, employing both Full Shape and Shape fit methodologies. We explore three possible values of the minimum scale, namely $s_{\min} = 22, h^{-1}\text{Mpc}$, $s_{\min} = 30, h^{-1}\text{Mpc}$, and $s_{\min} = 38, h^{-1}\text{Mpc}$. We found that both methodologies are in good agreement with each other and with the true values of the simulation for all minimum scales explored and for all parameters within 1σ . Given that the smaller scale corresponds to tighter constraints, we select $s_{\min} = 22, h^{-1}\text{Mpc}$ as the baseline value utilized throughout the rest of this work. We have also tested how our methodology is affected by switching between the minimal and maximal freedom scenarios, where b_{s^2} is either set free

or fixed to zero, and we define maximal freedom as our baseline configuration. We found that while all predictions are consistent within 1σ for V_1 , the minimal freedom case yields constraints approximately 10% tighter. This improvement in constraining power is expected when one reduces the parameter space explored.

In this work, we have also analyzed several extensions to our standard configuration. The first of these extensions is the inclusion of the hexadecapole of the correlation function into our analysis, which is considered as the multipole where first-loop PT starts to find difficulties modeling our scales of interest. In this extension, we include a model of the hexadecapole but only down to a minimum scale of $s_{\rm min} = 30\,h^{-1}{\rm Mpc}$ as we do not trust our model at smaller scales. We note that this extension does not significantly improve our results, with its only advantage being a small improvement in the precision of the *Full Modeling* estimates. We also highlight that all predictions recover the true value of all parameters within 1σ .

We have explored the inclusion of the spectral index n_s into our methodology as another extension to our model and analyzed how this affects the fits on the LRG sample using the Full Shape configuration of our model. We found that our model predicts all parameters, including n_s , to within 1σ . Additionally, we observe that the ability to recover the original parameters improves over their baseline counterparts at all scales. It is noteworthy that under this extension, our minimum scale of $s_{\min} = 30 \, h^{-1}{\rm Mpc}$ shows the best performance overall.

As another extension to our baseline analysis we have expanded our standard setup to include the w_0 and w_a parameters of the Chevallier–Polarski–Linder model of dark energy. We run our fitting methodology on our LRG sample and for two distinct configurations of these extensions, first we allow for only w_0 to vary while keeping w_a fixed at its true values. Then we allow both parameters to vary simultaneously. We find that all constrains using our Full-Modeling configuration are capable of recovering the ABACUS–SUMMIT parameters, including w_0 and w_a well bellow the 1σ range, we also note that in both cases the $s_{\min} = 22 \, h^{-1}{\rm Mpc}$ shows the overall best performance. We believe the accuracy of our fits is in part a result of working in CS, where volume effects play a smaller role on these new parameters.

All the tests and extensions discussed so far have been analyzed using our LRG sample. As a separate test, we have analyzed the accuracy of our methodology when fitting the QSO and ELG samples from ABACUS-SUMMIT. We have conducted fits for these two new samples using our standard configuration for three different minimum scales. In general, we observe that the ELG fits are slightly more accurate and precise than the LRG fits, while the QSO fits are generally less precise. This discrepancy is expected due to the differences in the number of tracers between the samples. Nevertheless, our methodology successfully recovers all parameters within 1σ for all three samples. Additionally, we find that using a minimum scale of $s_{\min} = 22, h^{-1}$ Mpc provides tighter constraints on our parameter space while also predicting all parameters precisely.

We have also conducted tests comparing the performance of Full Modeling and ShapeFit within cosmological parameter space. They involved examining the impact of variations in certain settings, including bias settings and minimum scale ranges. Additionally, we explored how these configurations were affected by our three model extensions: hexadecapole and n_s free. We observed that the various configurations of our vanilla model generally exhibit agreement in their estimates of the central values between both methodologies. There are slight variations in the size of their error estimates, ranging from a few to 30 percent depending on the case studied and the specific parameter. On the other hand, when considering extensions beyond the baseline that involve varying additional cosmological parameters, we observed larger disparities in both the central values and the size of the error bars. Specif-

ically, when allowing n_s to vary freely, we found that the *Full Modeling* approach imposes greater constraints, particularly on n_s compared to *ShapeFit*.

The last tests we have presented analyze the performance of our CS methodology, GSM-EFT, when compared to three FS codes: Velocileptors, Folps ν , and PyBird. This analysis serves as a complement to the main comparison between RSD methodologies presented in a companion paper dedicated to the consistency of all FS models. We found that our GSM-EFT results are in good agreement with those from all FS models, with our results showing smaller error bars for both Full Modeling and ShapeFit configurations. We have also investigated the performance of models in CS through the common framework desilike, confirming the aforementioned consistency of models in both spaces and the reduction of error bars in CS.

8 Data Availability

The data will be made publicly available once the paper is accepted.

Acknowledgments

SR, HN, SF, FR and MV are supported by Investigacion in Ciencia Basica CONAHCYT grant No. A1-S-13051 and PAPIIT IN108321 and IN116024, and Proyecto PIFF. SF and FR is supported by PAPIIT IN115424. HN and AA are supported by Ciencia de Frontera grant No. 319359 and PAPIIT IG102123.

MIL recognizes the support of the National Research Foundation of Korea (NRF) grant funded by the Korea government (MIST), Grant No. 2021R1A2C1013024

This material is based upon work supported by the U.S. Department of Energy (DOE), Office of Science, Office of High-Energy Physics, under Contract No. DE—AC02—05CH11231, and by the National Energy Research Scientific Computing Center, a DOE Office of Science User Facility under the same contract. Additional support for DESI was provided by the U.S. National Science Foundation (NSF), Division of Astronomical Sciences under Contract No. AST-0950945 to the NSF's National Optical-Infrared Astronomy Research Laboratory; the Science and Technology Facilities Council of the United Kingdom; the Gordon and Betty Moore Foundation; the Heising-Simons Foundation; the French Alternative Energies and Atomic Energy Commission (CEA); the National Council of Humanities, Science and Technology of Mexico (CONAHCYT); the Ministry of Science and Innovation of Spain (MICINN), and by the DESI Member Institutions: https://www.desi.lbl.gov/collaborating-institutions. Any opinions, findings, and conclusions or recommendations expressed in this material are those of the author(s) and do not necessarily reflect the views of the U.S. National Science Foundation, the U.S. Department of Energy, or any of the listed funding agencies.

The authors are honored to be permitted to conduct scientific research on Iolkam Du'ag (Kitt Peak), a mountain with particular significance to the Tohono O'odham Nation.

A Author Affiliations

 1 Instituto de Física, Universidad Nacional Autónoma de México, Cd. de México C.P. 04510, México

- ²Korea Astronomy and Space Science Institute, 776, Daedeokdae-ro, Yuseong-gu, Daejeon 34055, Republic of Korea
- ³Instituto de Ciencias Físicas, Universidad Autónoma de México, Cuernavaca, Morelos, 62210, (México)
- ⁴Lawrence Berkeley National Laboratory, 1 Cyclotron Road, Berkeley, CA 94720, USA
- ⁵Physics Dept., Boston University, 590 Commonwealth Avenue, Boston, MA 02215, USA
- ⁶University of Michigan, Ann Arbor, MI 48109, USA
- ⁷Institute for Astronomy, University of Edinburgh, Royal Observatory, Blackford Hill, Edinburgh EH9 3HJ, UK
- ⁸Department of Physics & Astronomy, University College London, Gower Street, London, WC1E 6BT, UK
- ⁹Institute for Computational Cosmology, Department of Physics, Durham University, South Road, Durham DH1 3LE, UK
- ¹⁰NSF NOIRLab, 950 N. Cherry Ave., Tucson, AZ 85719, USA
- ¹¹Department of Physics & Astronomy and Pittsburgh Particle Physics, Astrophysics, and Cosmology Center (PITT PACC), University of Pittsburgh, 3941 O'Hara Street, Pittsburgh, PA 15260, USA
- ¹²Kavli Institute for Particle Astrophysics and Cosmology, Stanford University, Menlo Park, CA 94305, USA
- ¹³SLAC National Accelerator Laboratory, Menlo Park, CA 94305, USA
- ¹⁴Departamento de Física, Universidad de los Andes, Cra. 1 No. 18A-10, Edificio Ip, CP 111711, Bogotá, Colombia
- ¹⁵Observatorio Astronómico, Universidad de los Andes, Cra. 1 No. 18A-10, Edificio H, CP 111711 Bogotá, Colombia
- ¹⁶Institut d'Estudis Espacials de Catalunya (IEEC), 08034 Barcelona, Spain
- ¹⁷Institute of Cosmology and Gravitation, University of Portsmouth, Dennis Sciama Building, Portsmouth, PO1 3FX, UK
- 18 Institute of Space Sciences, ICE-CSIC, Campus UAB, Carrer de Can Magrans s/n, 08913 Bellaterra, Barcelona, Spain
- ¹⁹Departament de Física Quàntica i Astrofísica, Universitat de Barcelona, Martí i Franquès 1, E08028 Barcelona, Spain
- ²⁰Institut de Ciències del Cosmos (ICCUB), Universitat de Barcelona (UB), c. Martí i Franquès, 1, 08028 Barcelona, Spain.
- ²¹Center for Cosmology and AstroParticle Physics, The Ohio State University, 191 West Woodruff Avenue, Columbus, OH 43210, USA
- $^{22}\mbox{Department}$ of Physics, The Ohio State University, 191 West Woodruff Avenue, Columbus, OH 43210, USA
- ²³The Ohio State University, Columbus, 43210 OH, USA
- ²⁴School of Mathematics and Physics, University of Queensland, 4072, Australia
- ²⁵Departament de Física, Serra Húnter, Universitat Autònoma de Barcelona, 08193 Bellaterra (Barcelona), Spain
- ²⁶Institut de Física d'Altes Energies (IFAE), The Barcelona Institute of Science and Technology, Campus UAB, 08193 Bellaterra Barcelona, Spain
- ²⁷University of California, Berkeley, 110 Sproul Hall #5800 Berkeley, CA 94720, USA
- ²⁸Institució Catalana de Recerca i Estudis Avançats, Passeig de Lluís Companys, 23, 08010 Barcelona, Spain
- ²⁹Department of Physics and Astronomy, University of Sussex, Brighton BN1 9QH, U.K

- ³⁰Department of Physics & Astronomy, University of Wyoming, 1000 E. University, Dept. 3905, Laramie, WY 82071, USA
- ³¹National Astronomical Observatories, Chinese Academy of Sciences, A20 Datun Rd., Chaoyang District, Beijing, 100012, P.R. China
- ³²Department of Physics and Astronomy, University of Waterloo, 200 University Ave W, Waterloo, ON N2L 3G1, Canada
- ³³Perimeter Institute for Theoretical Physics, 31 Caroline St. North, Waterloo, ON N2L 2Y5, Canada
- ³⁴Waterloo Centre for Astrophysics, University of Waterloo, 200 University Ave W, Waterloo, ON N2L 3G1, Canada
- ³⁵Space Sciences Laboratory, University of California, Berkeley, 7 Gauss Way, Berkeley, CA 94720, USA
- ³⁶Department of Physics, Kansas State University, 116 Cardwell Hall, Manhattan, KS 66506, USA
- ³⁷Department of Physics and Astronomy, Sejong University, Seoul, 143-747, Korea
- ³⁸CIEMAT, Avenida Complutense 40, E-28040 Madrid, Spain
- ³⁹Department of Physics, University of Michigan, Ann Arbor, MI 48109, USA
- ⁴⁰Department of Physics & Astronomy, Ohio University, Athens, OH 45701, USA
- ⁴¹Physics Department, Stanford University, Stanford, CA 93405, USA
- ⁴²Sorbonne Université, CNRS/IN2P3, Laboratoire de Physique Nucléaire et de Hautes Energies (LPNHE), FR-75005 Paris, France

References

- [1] M. Colless, G. Dalton, S. Maddox, W. Sutherland, P. Norberg, S. Cole et al., *The 2dF Galaxy Redshift Survey: spectra and redshifts*, *MNRAS* **328** (Dec., 2001) 1039–1063, [astro-ph/0106498].
- [2] W. J. Percival, C. M. Baugh, J. Bland-Hawthorn, T. Bridges, R. Cannon, S. Cole et al., The 2dF Galaxy Redshift Survey: the power spectrum and the matter content of the Universe, MNRAS 327 (Nov., 2001) 1297–1306, [astro-ph/0105252].
- [3] K. S. Dawson, D. J. Schlegel, C. P. Ahn, S. F. Anderson, É. Aubourg, S. Bailey et al., *The Baryon Oscillation Spectroscopic Survey of SDSS-III*, *AJ* 145 (Jan., 2013) 10, [1208.0022].
- [4] S. Alam, M. Ata, S. Bailey, F. Beutler, D. Bizyaev, J. A. Blazek et al., The clustering of galaxies in the completed SDSS-III Baryon Oscillation Spectroscopic Survey: cosmological analysis of the DR12 galaxy sample, MNRAS 470 (Sept., 2017) 2617–2652, [1607.03155].
- [5] K. S. Dawson, J.-P. Kneib, W. J. Percival, S. Alam, F. D. Albareti, S. F. Anderson et al., The SDSS-IV Extended Baryon Oscillation Spectroscopic Survey: Overview and Early Data, AJ 151 (Feb., 2016) 44, [1508.04473].
- [6] S. Alam, M. Aubert, S. Avila, C. Balland, J. E. Bautista, M. A. Bershady et al., Completed SDSS-IV extended Baryon Oscillation Spectroscopic Survey: Cosmological implications from two decades of spectroscopic surveys at the Apache Point Observatory, PRD 103 (Apr., 2021) 083533, [2007.08991].
- [7] J. Zuntz, E. Sheldon, S. Samuroff, M. A. Troxel, M. Jarvis, N. MacCrann et al., Dark Energy Survey Year 1 results: weak lensing shape catalogues, MNRAS 481 (Nov., 2018) 1149–1182, [1708.01533].
- [8] T. M. C. Abbott, F. B. Abdalla, A. Alarcon, J. Aleksić, S. Allam, S. Allen et al., Dark Energy Survey year 1 results: Cosmological constraints from galaxy clustering and weak lensing, PRD 98 (Aug., 2018) 043526, [1708.01530].

- [9] R. Laureijs, J. Amiaux, S. Arduini, J. L. Auguères, J. Brinchmann, R. Cole et al., *Euclid Definition Study Report*, arXiv e-prints (Oct., 2011) arXiv:1110.3193, [1110.3193].
- [10] G. D. Racca, R. Laureijs, L. Stagnaro, J.-C. Salvignol, J. Lorenzo Alvarez, G. Saavedra Criado et al., The Euclid mission design, in Space Telescopes and Instrumentation 2016: Optical, Infrared, and Millimeter Wave (H. A. MacEwen, G. G. Fazio, M. Lystrup, N. Batalha, N. Siegler and E. C. Tong, eds.), vol. 9904 of Society of Photo-Optical Instrumentation Engineers (SPIE) Conference Series, p. 990400, July, 2016. 1610.05508. DOI.
- [11] Ż. Ivezić, S. M. Kahn, J. A. Tyson, B. Abel, E. Acosta, R. Allsman et al., LSST: From Science Drivers to Reference Design and Anticipated Data Products, Ap.J 873 (Mar., 2019) 111, [0805.2366].
- [12] DESI Collaboration, A. Aghamousa, J. Aguilar, S. Ahlen, S. Alam, L. E. Allen et al., *The DESI Experiment Part I: Science, Targeting, and Survey Design, arXiv e-prints* (Oct., 2016) arXiv:1611.00036, [1611.00036].
- [13] DESI Collaboration, B. Abareshi, J. Aguilar, S. Ahlen, S. Alam, D. M. Alexander et al., Overview of the Instrumentation for the Dark Energy Spectroscopic Instrument, AJ 164 (Nov., 2022) 207, [2205.10939].
- [14] DESI Collaboration, A. G. Adame, J. Aguilar, S. Ahlen, S. Alam, G. Aldering et al., Validation of the Scientific Program for the Dark Energy Spectroscopic Instrument, AJ 167 (Feb., 2024) 62, [2306.06307].
- [15] DESI Collaboration, A. G. Adame, J. Aguilar, S. Ahlen, S. Alam, G. Aldering et al., The Early Data Release of the Dark Energy Spectroscopic Instrument, arXiv e-prints (June, 2023) arXiv:2306.06308, [2306.06308].
- [16] D. J. Schlegel, S. Ferraro, G. Aldering, C. Baltay, S. BenZvi, R. Besuner et al., A Spectroscopic Road Map for Cosmic Frontier: DESI, DESI-II, Stage-5, arXiv e-prints (Sept., 2022) arXiv:2209.03585, [2209.03585].
- [17] A. Raichoor, D. J. Eisenstein, T. Karim, J. A. Newman, J. Moustakas, D. D. Brooks et al., Preliminary Target Selection for the DESI Emission Line Galaxy (ELG) Sample, Research Notes of the American Astronomical Society 4 (Oct., 2020) 180, [2010.11281].
- [18] R. Zhou, J. A. Newman, K. S. Dawson, D. J. Eisenstein, D. D. Brooks, A. Dey et al., Preliminary Target Selection for the DESI Luminous Red Galaxy (LRG) Sample, Research Notes of the American Astronomical Society 4 (Oct., 2020) 181, [2010.11282].
- [19] C. Yèche, N. Palanque-Delabrouille, C.-A. Claveau, D. D. Brooks, E. Chaussidon, T. M. Davis et al., Preliminary Target Selection for the DESI Quasar (QSO) Sample, Research Notes of the American Astronomical Society 4 (Oct., 2020) 179, [2010.11280].
- [20] B. A. Reid, L. Samushia, M. White, W. J. Percival, M. Manera, N. Padmanabhan et al., The clustering of galaxies in the SDSS-III Baryon Oscillation Spectroscopic Survey: measurements of the growth of structure and expansion rate at z = 0.57 from anisotropic clustering, MNRAS 426 (Nov., 2012) 2719–2737, [1203.6641].
- [21] L. Samushia, B. A. Reid, M. White, W. J. Percival, A. J. Cuesta, G.-B. Zhao et al., The clustering of galaxies in the SDSS-III Baryon Oscillation Spectroscopic Survey: measuring growth rate and geometry with anisotropic clustering, MNRAS 439 (Apr., 2014) 3504–3519, [1312.4899].
- [22] S. Satpathy, S. Alam, S. Ho, M. White, N. A. Bahcall, F. Beutler et al., The clustering of galaxies in the completed SDSS-III Baryon Oscillation Spectroscopic Survey: on the measurement of growth rate using galaxy correlation functions, MNRAS 469 (Aug., 2017) 1369–1382, [1607.03148].
- [23] A. Tamone, A. Raichoor, C. Zhao, A. de Mattia, C. Gorgoni, E. Burtin et al., The completed SDSS-IV extended baryon oscillation spectroscopic survey: growth rate of structure

- measurement from anisotropic clustering analysis in configuration space between redshift 0.6 and 1.1 for the emission-line galaxy sample, MNRAS 499 (Dec., 2020) 5527–5546, [2007.09009].
- [24] S.-F. Chen, Z. Vlah and M. White, Consistent modeling of velocity statistics and redshift-space distortions in one-loop perturbation theory, JCAP 2020 (July, 2020) 062, [2005.00523].
- [25] Y. Zhang, A. R. Pullen, S. Alam, S. Singh, E. Burtin, C.-H. Chuang et al., Testing general relativity on cosmological scales at redshift $z \sim 1.5$ with quasar and CMB lensing, MNRAS 501 (Feb., 2021) 1013–1027, [2007.12607].
- [26] J. E. Bautista, R. Paviot, M. Vargas Magaña, S. de la Torre, S. Fromenteau, H. Gil-Marín et al., The completed SDSS-IV extended Baryon Oscillation Spectroscopic Survey: measurement of the BAO and growth rate of structure of the luminous red galaxy sample from the anisotropic correlation function between redshifts 0.6 and 1, MNRAS 500 (Jan., 2021) 736-762, [2007.08993].
- [27] L. Fonseca de la Bella, D. Regan, D. Seery and S. Hotchkiss, *The matter power spectrum in redshift space using effective field theory*, *JCAP* **2017** (Nov., 2017) 039, [1704.05309].
- [28] V. Desjacques, D. Jeong and F. Schmidt, *The galaxy power spectrum and bispectrum in redshift space*, *JCAP* **2018** (Dec., 2018) 035, [1806.04015].
- [29] A. Chudaykin, M. M. Ivanov, O. H. E. Philcox and M. Simonović, Nonlinear perturbation theory extension of the Boltzmann code CLASS, PRD 102 (Sept., 2020) 063533, [2004.10607].
- [30] G. d'Amico, J. Gleyzes, N. Kokron, K. Markovic, L. Senatore, P. Zhang et al., *The cosmological analysis of the SDSS/BOSS data from the Effective Field Theory of Large-Scale Structure*, *JCAP* **2020** (May, 2020) 005, [1909.05271].
- [31] P. McDonald, Clustering of dark matter tracers: Renormalizing the bias parameters, Phys. Rev. D 74 (2006) 103512, [astro-ph/0609413].
- [32] P. McDonald and A. Roy, Clustering of dark matter tracers: generalizing bias for the coming era of precision LSS, JCAP 08 (2009) 020, [0902.0991].
- [33] D. Baumann, A. Nicolis, L. Senatore and M. Zaldarriaga, Cosmological Non-Linearities as an Effective Fluid, JCAP 07 (2012) 051, [1004.2488].
- [34] J. J. M. Carrasco, M. P. Hertzberg and L. Senatore, The Effective Field Theory of Cosmological Large Scale Structures, JHEP 09 (2012) 082, [1206.2926].
- [35] Z. Vlah, M. White and A. Aviles, A Lagrangian effective field theory, JCAP **09** (2015) 014, [1506.05264].
- [36] S.-F. Chen, Z. Vlah, E. Castorina and M. White, *Redshift-space distortions in Lagrangian perturbation theory*, *JCAP* **2021** (Mar., 2021) 100, [2012.04636].
- [37] T. Matsubara, Resumming Cosmological Perturbations via the Lagrangian Picture: One-loop Results in Real Space and in Redshift Space, Phys. Rev. D 77 (2008) 063530, [0711.2521].
- [38] J. Carlson, B. Reid and M. White, Convolution Lagrangian perturbation theory for biased tracers, Mon. Not. Roy. Astron. Soc. 429 (2013) 1674, [1209.0780].
- [39] Z. Vlah, E. Castorina and M. White, The Gaussian streaming model and convolution Lagrangian effective field theory, JCAP 12 (2016) 007, [1609.02908].
- [40] A. Aviles, Renormalization of Lagrangian bias via spectral parameters, Phys. Rev. D 98 (2018) 083541, [1805.05304].
- [41] N. A. Maksimova, L. H. Garrison, D. J. Eisenstein, B. Hadzhiyska, S. Bose and T. P. Satterthwaite, ABACUSSUMMIT: a massive set of high-accuracy, high-resolution N-body simulations, MNRAS 508 (Dec., 2021) 4017–4037, [2110.11398].

- [42] S. Ramirez, M. Icaza-Lizaola, S. Fromenteau, M. Vargas-Magaña and A. Aviles, Full Shape Cosmology Analysis from BOSS in configuration space using Neural Network Acceleration, arXiv e-prints (Oct., 2023) arXiv:2310.17834, [2310.17834].
- [43] G. d'Amico, J. Gleyzes, N. Kokron, K. Markovic, L. Senatore, P. Zhang et al., The cosmological analysis of the SDSS/BOSS data from the Effective Field Theory of Large-Scale Structure, JCAP 2020 (May, 2020) 005, [1909.05271].
- [44] T. Colas, G. d'Amico, L. Senatore, P. Zhang and F. Beutler, Efficient cosmological analysis of the SDSS/BOSS data from the Effective Field Theory of Large-Scale Structure, JCAP 2020 (June, 2020) 001, [1909.07951].
- [45] G. D'Amico, L. Senatore and P. Zhang, Limits on wCDM from the EFTofLSS with the PyBird code, JCAP 2021 (Jan., 2021) 006, [2003.07956].
- [46] Y. Lai, C. Howlett, M. Maus, H. Gil-Marín, H. E. Noriega, S. Ramírez-Solano et al., A comparison between Shapefit compression and Full-Modelling method with PyBird for DESI 2024 and beyond, arXiv e-prints (2024) arXiv:2404.07283, [2404.07283].
- [47] H. E. Noriega, A. Aviles, S. Fromenteau and M. Vargas-Magaña, Fast computation of non-linear power spectrum in cosmologies with massive neutrinos, JCAP 2022 (Nov., 2022) 038, [2208.02791].
- [48] H. E. Noriega, A. Aviles, H. Gil-Marín, S. Ramirez-Solano, S. Fromenteau, M. Vargas-Magaña et al., Comparing compressed and full-modeling analyses with folps: Implications for desi 2024 and beyond, arXiv e-prints (2024) arXiv:2404.07269, [2404.07269].
- [49] S.-F. Chen, Z. Vlah, E. Castorina and M. White, Redshift-space distortions in Lagrangian perturbation theory, JCAP 2021 (Mar., 2021) 100, [2012.04636].
- [50] S.-F. Chen, Z. Vlah and M. White, Consistent modeling of velocity statistics and redshift-space distortions in one-loop perturbation theory, JCAP 2020 (July, 2020) 062, [2005.00523].
- [51] M. Maus, S. Chen, M. White, J. Aguilar, S. Ahlen, A. Aviles et al., An analysis of parameter compression and full-modeling techniques with Velocileptors for DESI 2024 and beyond, arXiv e-prints (2024) arXiv:2404.07312, [2404.07312].
- [52] M. Maus, Y. Lai, H. E. Noriega, S. Ramirez-Solano, A. Aviles, S. Chen et al., A comparison of effective field theory models of redshift space galaxy power spectra for desi 2024 and future surveys, arXiv e-prints (2024) arXiv:2404.07272, [2404.07272].
- [53] K. B. Fisher, On the validity of the streaming model for the redshift space correlation function in the linear regime, Astrophys. J. 448 (1995) 494-499, [astro-ph/9412081].
- [54] R. Scoccimarro, Redshift-space distortions, pairwise velocities and nonlinearities, Phys. Rev. D70 (2004) 083007, [astro-ph/0407214].
- [55] B. A. Reid and M. White, Towards an accurate model of the redshift space clustering of halos in the quasilinear regime, Mon. Not. Roy. Astron. Soc. 417 (2011) 1913–1927, [1105.4165].
- [56] L. Wang, B. Reid and M. White, An analytic model for redshift-space distortions, Mon. Not. Roy. Astron. Soc. 437 (2014) 588–599, [1306.1804].
- [57] D. J. Eisenstein, D. H. Weinberg, E. Agol, H. Aihara, C. Allende Prieto, S. F. Anderson et al., SDSS-III: Massive Spectroscopic Surveys of the Distant Universe, the Milky Way, and Extra-Solar Planetary Systems, AJ 142 (Sept., 2011) 72, [1101.1529].
- [58] S. Alam, F. D. Albareti, C. Allende Prieto, F. Anders, S. F. Anderson, T. Anderton et al., The Eleventh and Twelfth Data Releases of the Sloan Digital Sky Survey: Final Data from SDSS-III, ApJS 219 (July, 2015) 12, [1501.00963].
- [59] A. Raichoor, A. de Mattia, A. J. Ross, C. Zhao, S. Alam, S. Avila et al., The completed SDSS-IV extended Baryon Oscillation Spectroscopic Survey: large-scale structure catalogues

- and measurement of the isotropic BAO between redshift 0.6 and 1.1 for the Emission Line Galaxy Sample, MNRAS **500** (Jan., 2021) 3254–3274, [2007.09007].
- [60] A. J. Ross, J. Bautista, R. Tojeiro, S. Alam, S. Bailey, E. Burtin et al., The Completed SDSS-IV extended Baryon Oscillation Spectroscopic Survey: Large-scale structure catalogues for cosmological analysis, MNRAS 498 (Oct., 2020) 2354–2371, [2007.09000].
- [61] B. W. Lyke, A. N. Higley, J. N. McLane, D. P. Schurhammer, A. D. Myers, A. J. Ross et al., The Sloan Digital Sky Survey Quasar Catalog: Sixteenth Data Release, ApJS 250 (Sept., 2020) 8, [2007.09001].
- [62] C. Alcock and B. Paczynski, An evolution free test for non-zero cosmological constant, Nature **281** (Oct., 1979) 358.
- [63] S. Brieden, H. Gil-Marín and L. Verde, ShapeFit: extracting the power spectrum shape information in galaxy surveys beyond BAO and RSD, JCAP 2021 (Dec., 2021) 054, [2106.07641].
- [64] A. G. Sánchez, R. Scoccimarro, M. Crocce, J. N. Grieb, S. Salazar-Albornoz, C. Dalla Vecchia et al., The clustering of galaxies in the completed SDSS-III Baryon Oscillation Spectroscopic Survey: Cosmological implications of the configuration-space clustering wedges, MNRAS 464 (Jan., 2017) 1640–1658, [1607.03147].
- [65] J. N. Grieb, A. G. Sánchez, S. Salazar-Albornoz, R. Scoccimarro, M. Crocce, C. Dalla Vecchia et al., The clustering of galaxies in the completed SDSS-III Baryon Oscillation Spectroscopic Survey: Cosmological implications of the Fourier space wedges of the final sample, MNRAS 467 (May, 2017) 2085–2112, [1607.03143].
- [66] A. Semenaite, A. G. Sánchez, A. Pezzotta, J. Hou, R. Scoccimarro, A. Eggemeier et al., Cosmological implications of the full shape of anisotropic clustering measurements in BOSS and eBOSS, MNRAS 512 (June, 2022) 5657–5670, [2111.03156].
- [67] R. Neveux, E. Burtin, V. Ruhlmann-Kleider, A. de Mattia, A. Semenaite, K. S. Dawson et al., Combined full shape analysis of BOSS galaxies and eBOSS quasars using an iterative emulator, MNRAS 516 (Oct., 2022) 1910–1922, [2201.04679].
- [68] DESI Collaboration, DESI 2024 V: Analysis of the full shape of two-point clustering statistics from galaxies and quasars, in preparation (2024).
- [69] DESI Collaboration, DESI 2024 I: Data Release 1 of the Dark Energy Spectroscopic Instrument, in preparation (2025).
- [70] DESI Collaboration, DESI 2024 II: Sample definitions, characteristics and two-point clustering statistics, in preparation (2024) .
- [71] DESI Collaboration, A. G. Adame, J. Aguilar, S. Ahlen, S. Alam, D. M. Alexander et al., DESI 2024 III: Baryon Acoustic Oscillations from Galaxies and Quasars, arXiv e-prints (2024) arXiv:2404.03000, [2404.03000].
- [72] DESI Collaboration, A. G. Adame, J. Aguilar, S. Ahlen, S. Alam, D. M. Alexander et al., DESI 2024 IV: Baryon Acoustic Oscillations from the Lyman Alpha Forest, arXiv e-prints (2024) arXiv:2404.03001, [2404.03001].
- [73] DESI Collaboration, DESI 2024 VII: Cosmological constraints from full-shape analyses of the two-point clustering statistics measurements, in preparation (2024).
- [74] DESI Collaboration, DESI 2024 VIII: Constraints on Primordial Non-Gaussianities, in preparation (2024) .
- [75] Planck Collaboration, N. Aghanim, Y. Akrami, M. Ashdown, J. Aumont, C. Baccigalupi et al., Planck 2018 results. VI. Cosmological parameters, A&A 641 (Sept., 2020) A6, [1807.06209].

- [76] A. Rocher, V. Ruhlmann-Kleider, E. Burtin and A. de Mattia, Halo occupation distribution of Emission Line Galaxies: fitting method with Gaussian processes, JCAP 2023 (May, 2023) 033, [2302.07056].
- [77] S. Yuan, H. Zhang, A. J. Ross, J. Donald-McCann, B. Hadzhiyska, R. H. Wechsler et al., The DESI One-Percent Survey: Exploring the Halo Occupation Distribution of Luminous Red Galaxies and Quasi-Stellar Objects with AbacusSummit, arXiv e-prints (June, 2023) arXiv:2306.06314, [2306.06314].
- [78] C.-H. Chuang, F.-S. Kitaura, F. Prada, C. Zhao and G. Yepes, EZmocks: extending the Zel'dovich approximation to generate mock galaxy catalogues with accurate clustering statistics, Monthly Notices of the Royal Astronomical Society 446 (11, 2014) 2621-2628, [https://academic.oup.com/mnras/article-pdf/446/3/2621/10448149/stu2301.pdf].
- [79] S. Ramirez, M. Icaza-Lizaola, S. Fromenteau, M. Vargas-Magaña and A. Aviles, Full Shape Cosmology Analysis from BOSS in configuration space using Neural Network Acceleration, arXiv e-prints (Oct., 2023) arXiv:2310.17834, [2310.17834].
- [80] Z. Vlah and M. White, Exploring redshift-space distortions in large-scale structure, JCAP 1903 (2019) 007, [1812.02775].
- [81] T. Matsubara, Nonlinear perturbation theory with halo bias and redshift-space distortions via the Lagrangian picture, Phys. Rev. D 78 (2008) 083519, [0807.1733].
- [82] C. Uhlemann, M. Kopp and T. Haugg, Edgeworth streaming model for redshift space distortions, Phys. Rev. D 92 (2015) 063004, [1503.08837].
- [83] G. Valogiannis, R. Bean and A. Aviles, An accurate perturbative approach to redshift space clustering of biased tracers in modified gravity, JCAP 2020 (Jan., 2020) 055, [1909.05261].
- [84] J. DeRose, S.-F. Chen, M. White and N. Kokron, Neural network acceleration of large-scale structure theory calculations, JCAP 2022 (Apr., 2022) 056, [2112.05889].
- [85] J. Alsing, H. Peiris, J. Leja, C. Hahn, R. Tojeiro, D. Mortlock et al., SPECULATOR: Emulating Stellar Population Synthesis for Fast and Accurate Galaxy Spectra and Photometry, ApJS 249 (July, 2020) 5, [1911.11778].
- [86] A. Korobov, The approximate computation of multiple integrals, in Dokl. Akad. Nauk SSSR, vol. 124, pp. 1207–1210, 1959.
- [87] M. Icaza-Lizaola, M. Vargas-Magaña, S. Fromenteau, S. Alam, B. Camacho, H. Gil-Marin et al., The clustering of the SDSS-IV extended Baryon Oscillation Spectroscopic Survey DR14 LRG sample: structure growth rate measurement from the anisotropic LRG correlation function in the redshift range 0.6 < z < 1.0, MNRAS 492 (Mar., 2020) 4189-4215, [1909.07742].</p>
- [88] M. M. Ivanov, M. Simonović and M. Zaldarriaga, Cosmological Parameters from the BOSS Galaxy Power Spectrum, JCAP 05 (2020) 042, [1909.05277].
- [89] G. D'Amico, J. Gleyzes, N. Kokron, K. Markovic, L. Senatore, P. Zhang et al., The Cosmological Analysis of the SDSS/BOSS data from the Effective Field Theory of Large-Scale Structure, JCAP 05 (2020) 005, [1909.05271].
- [90] O. H. E. Philcox, M. M. Ivanov, M. Simonović and M. Zaldarriaga, Combining full-shape and BAO analyses of galaxy power spectra: a 1.6% CMB-independent constraint on H₀, JCAP 2020 (May, 2020) 032, [2002.04035].
- [91] T. Tröster, A. G. Sánchez, M. Asgari, C. Blake, M. Crocce, C. Heymans et al., Cosmology from large-scale structure. Constraining ΛCDM with BOSS, A&A 633 (Jan., 2020) L10, [1909.11006].

- [92] S.-F. Chen, Z. Vlah and M. White, A new analysis of galaxy 2-point functions in the BOSS survey, including full-shape information and post-reconstruction BAO, JCAP **2022** (Feb., 2022) 008, [2110.05530].
- [93] A. Semenaite, A. G. Sánchez, A. Pezzotta, J. Hou, A. Eggemeier, M. Crocce et al., Beyond -ΛCDM constraints from the full shape clustering measurements from BOSS and eBOSS, MNRAS 521 (June, 2023) 5013–5025, [2210.07304].
- [94] S. Brieden, H. Gil-Marín and L. Verde, ShapeFit: extracting the power spectrum shape information in galaxy surveys beyond BAO and RSD, JCAP 2021 (Dec., 2021) 054, [2106.07641].
- [95] S. Brieden, H. Gil-Marín and L. Verde, Model-independent versus model-dependent interpretation of the SDSS-III BOSS power spectrum: Bridging the divide, PRD 104 (Dec., 2021) L121301, [2106.11931].
- [96] S. Brieden, H. Gil-Marín and L. Verde, PT challenge: validation of ShapeFit on large-volume, high-resolution mocks, JCAP 2022 (June, 2022) 005, [2201.08400].
- [97] S. Brieden, H. Gil-Marín and L. Verde, Model-agnostic interpretation of 10 billion years of cosmic evolution traced by BOSS and eBOSS data, JCAP 2022 (Aug., 2022) 024, [2204.11868].
- [98] D. J. Eisenstein and W. Hu, Power Spectra for Cold Dark Matter and Its Variants, ApJ 511 (Jan., 1999) 5–15, [astro-ph/9710252].
- [99] S.-F. Chen, Z. Vlah and M. White, Consistent Modeling of Velocity Statistics and Redshift-Space Distortions in One-Loop Perturbation Theory, JCAP 07 (2020) 062, [2005.00523].
- [100] S.-F. Chen, Z. Vlah, E. Castorina and M. White, Redshift-Space Distortions in Lagrangian Perturbation Theory, JCAP 03 (2021) 100, [2012.04636].
- [101] R. J. Cooke, M. Pettini and C. C. Steidel, One Percent Determination of the Primordial Deuterium Abundance, Ap.J. 855 (Mar., 2018) 102, [1710.11129].
- [102] D. Foreman-Mackey, D. W. Hogg, D. Lang and J. Goodman, emcee: The MCMC Hammer, Publ. Astron. Soc. Pac. 125 (2013) 306–312, [1202.3665].
- [103] J. Goodman and J. Weare, Ensemble samplers with affine invariance, Communications in Applied Mathematics and Computational Science 5 (Jan., 2010) 65–80.
- [104] C. Grove, C.-H. Chuang, N. C. Devi, L. Garrison, B. L'Huillier, Y. Feng et al., The DESI N-body simulation project I. Testing the robustness of simulations for the DESI dark time survey, MNRAS 515 (Sept., 2022) 1854–1870, [2112.09138].
- [105] M. Chevallier and D. Polarski, Accelerating Universes with Scaling Dark Matter, International Journal of Modern Physics D 10 (Jan., 2001) 213–223, [gr-qc/0009008].
- [106] E. V. Linder, Exploring the Expansion History of the Universe, PRL 90 (Mar., 2003) 091301, [astro-ph/0208512].

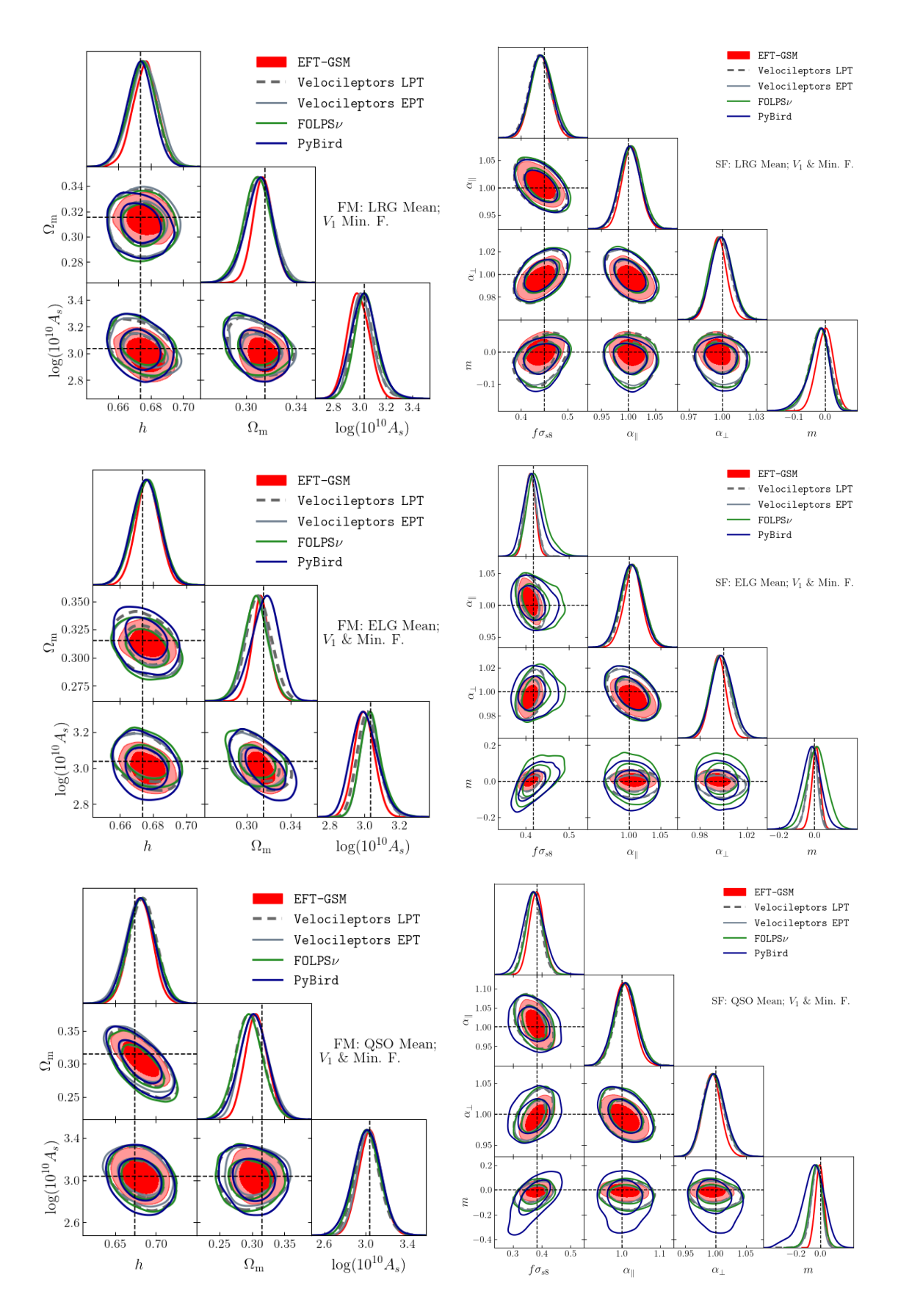


Figure 16. All models using their baseline analysis for all tracers. Need to replace left plots with the *Full Modeling* cases, change the format of the plot, i.e put in solid GSM-EFT

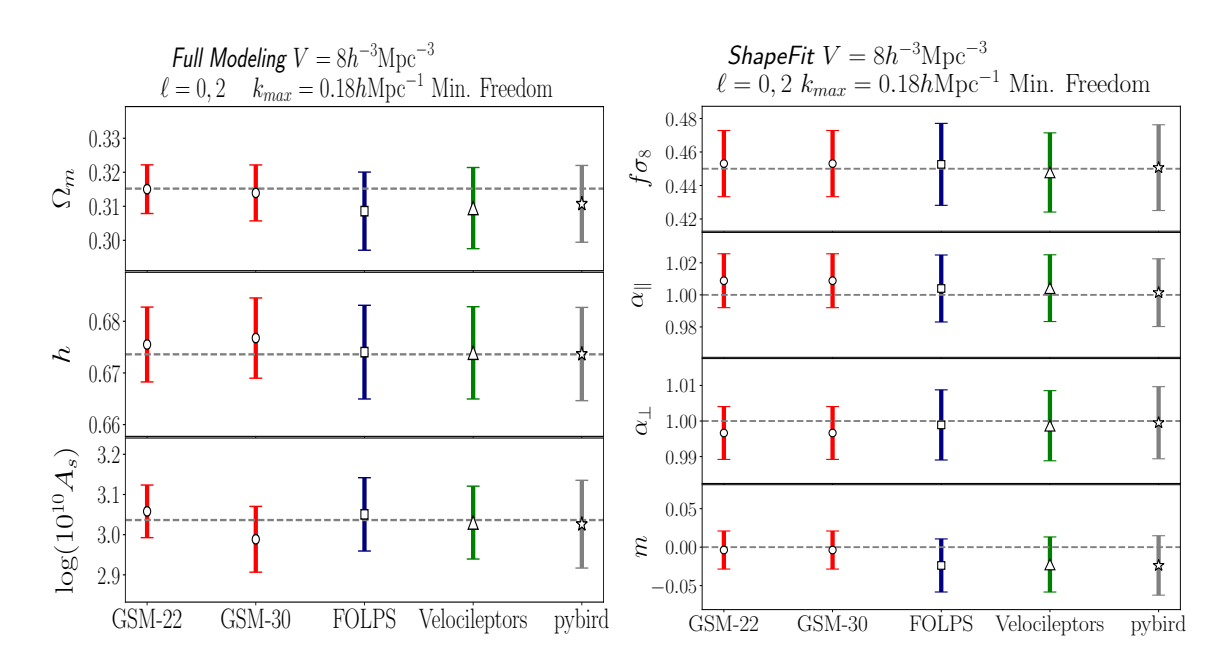


Figure 17. All models using their baseline analysis for the minimal freedom case with desilike

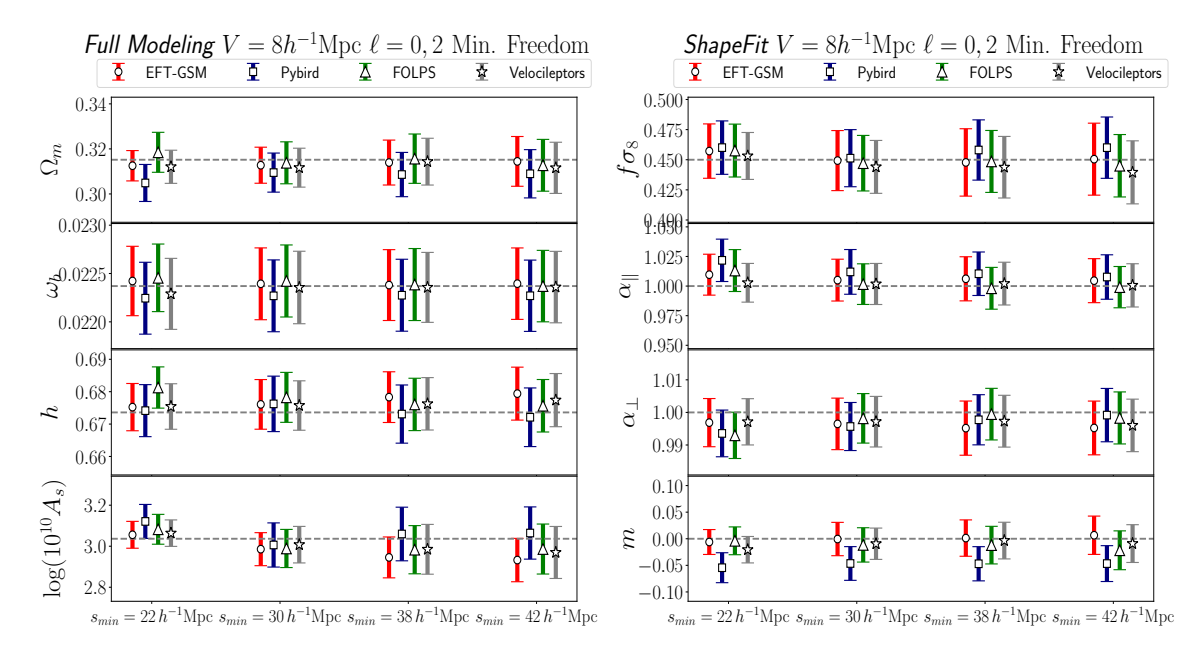


Figure 18. All models using their baseline analysis for the minimal freedom case.

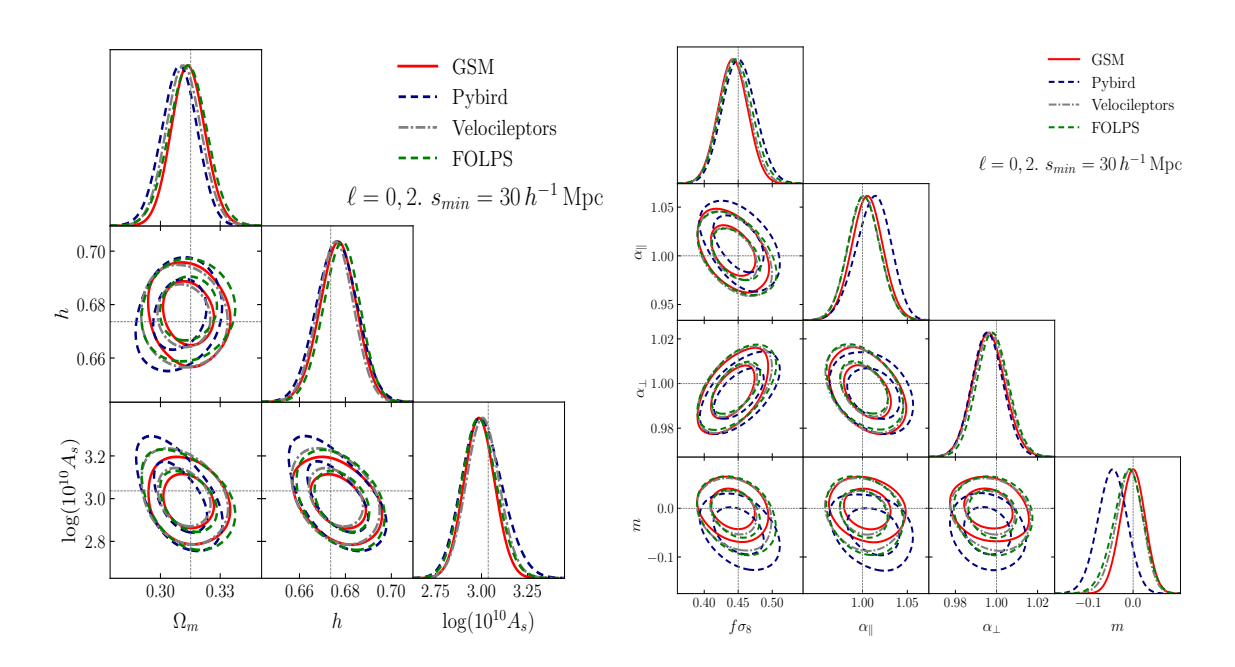


Figure 19. All models using their baseline analysis for the minimal freedom case for the correlation function.